Bachelorarbeit

Parton shower modelling uncertainty studies in entangled lepton+jets $t\bar{t}$ final states

Studien zu Modellierungsunsicherheiten in Teilchenschauern in verschränkten Lepton+Jets $t\bar{t}$ Endzuständen

angefertigt von

Tobias Henne

aus Göttingen

am II. Physikalisches Institut

Inhaltsverzeichnis

1 Introduction

More than 2000 years ago, the ancient greeks already contemplated the idea of smallest particles, "atoms", as building blocks of everything, that exists in the universe. It was not until the 1800s that a scientific foundation for the atomic model was laid through physics. Further discoveries revealed that the atom itself was an entity composed of even smaller particles. Today, the Standard Model of Particle Physics (SM) provides the basis for understanding these fundamental particles and their interactions.

The top quark is the heaviest of the elementary particles in the SM and as such possesses some unique properties, that make it a prime candidate for discovering new physics. It is the only quark that decays before forming a bound state and can therefore be used to study properties of bare quarks, such as entanglement. To study the particles of the the SM, high-energy particle accelerators such as the Large Hadron Collider (LHC) at CERN are used today. These machines collide particles at high energies to produce the different elementary particles and probe their interactions. To test the predictions made by the Standard Model or other physics models, one has to simulate the processes that occur after the collision takes place based on these models to be able to compare them to the actual data. Physicists use sophisticated programs called Monte Carlo Event Generators to handle this task. These generators incorporate fundamental theory combined with phenomenological models to simulate the collision events that are observed at particle detectors such as ATLAS at the LHC.

The modelling of top quark pairs using different event generators, namely PYTHIA and HERWIG, is studied in this thesis. In particular, a spin observable, which is sensitive to quantum entanglement, is introduced and the systematic uncertainties that emerge from the differences between the two generators are examined. The analysis focuses on the lepton+jets decay channel. A c-tagging approach is used in the construction of the spin observable and the event selection. The reconstruction of events simulating actual detector data is handled by the SPANet neural network. The differences in the SPANet reconstruction between PYTHIA and HERWIG are examined in greater detail.

2 Theory

This chapter lays the theoretical foundation for the analysis conducted in this thesis, including the Standard Model of Particle Physics, a short review of the top quark along with its unique properties with regard to quantum entanglement, and the generation of high-energy scattering events at particle colliders with a focus on parton showering.

2.1 The Standard Model of Particle Physics

The Standard Model is a quantum field theory that describes the elementary particles and their interactions through the electromagnetic, weak and strong forces.

2.1.1 Elementary Particles

The elementary particles of the SM can most generally be divided into integer spin bosons and spin $S = \frac{1}{2}$ fermions, with further differentiations within these categories using various quantum numbers. The bosons of the SM consist of spin $S = 1$ gauge bosons that mediate the aforementioned forces and the scalar-type Higgs boson with spin $S = 0$. The fermions of the SM obtain their mass through interaction with the Higgs field according to the strength of their Yukawa coupling to this field [1–4].

Fermions are the fundamental building blocks of matter. They can be divided into quarks that possess a colour charge and thus interact strongly and leptons that do not. There are six different flavours of quarks and leptons as shown in Figure 2.1. The up, charm, and top quark carry an electrical charge of $Q = +\frac{2}{3}$e and are classified as up-type quarks whereas the down, strange, and bottom quark carry an electrical charge of $Q = -\frac{1}{3}$e and are classified as down-type quarks. Leptons are similarly split into the electrically charged electron, muon, and tau each carrying a charge of $Q = -1$e and three electrically neutral neutrinos. Furthermore, for each fermion there exists a corresponding antiparticle of the same mass but opposite electric charge and flavour quantum number. Fermions have an additional vector-valued property called weak isospin which has a magnitude of $I = \frac{1}{2}$ for left-handed fermions or right-handed antifermions and $I = 0$ for opposite configurations. Notably, neutrinos have only ever been observed in the configurations

Abb. 2.1: A colour-coded overview of the elementary particles of the Standard Model with their mass, electric charge and spin. The three fermion generations are grouped as columns on the left. The force-carrying gauge bosons and the Higgs boson are depicted on the right side.

with $I = \frac{1}{2}$ [5]. Using the third component of the weak isospin I_3, quarks and leptons can be arranged into a weak isospin doublet for non-zero I, consisting of either an up-type quark or neutrino with $I_3 = +\frac{1}{2}$ on top and the corresponding down-type quark or charged lepton with $I_3 = -\frac{1}{2}$ on the bottom. As shown in Figure 2.1, the twelve elementary fermions can be further arranged into three generations according to their mass and flavour quantum numbers, each constisting of a quark and lepton weak isospin doublet. The electromagnetic and strong interaction properties of the particles do not change between generations. Only the up and down quark and electron of the first generation occur in stable matter as quarks and charged leptons of the higher generations decay into first generation particles through the weak interaction.

2.1.2 Fundamental Interactions

The Standard Model is a locally gauge-invariant quantum field theory with the underlying symmetry group $\mathrm{U}(1)_Y \times \mathrm{SU}(2)_L \times \mathrm{SU}(3)_C$ [6] where the aforementioned three fundamental forces are described by their respective gauge symmetries denoted by the subscripts. The force-carrying particles are therefore called gauge bosons. Furthermore, the SM is a renormalizable theory which guarantees finite cross sections for its interactions [7, 8].

The Electroweak Interaction

In the theory of Quantum Electrodynamics (QED) the local gauge symmetry U(1) corresponds to the electromagnetic interaction and gives rise to the force-carrying particle known as the photon. The photon mediates the electromagnetic force by coupling to the electric charge of a particle. As the symmetry group U(1) is Abelian, the photon does not interact with itself [6].

The local gauge symmetry $SU(2)_L$, where the L stands for left-handedness, describes the weak interaction in Quantum Flavourdynamics [6, 9, 10]. Since it has three generators, the weak force is mediated by three gauge bosons, namely the electrically charged $W^\pm$ bosons and the neutral Z^0 boson. Unlike QED, the generators do not commute with each other, making the $SU(2)_L$ group non-Abelian, which leads to self-interaction of its gauge bosons.

The W bosons couple to the third component of the weak isospin I_3. As a consequence, only left-handed particles and right-handed antiparticles interact through W exchange. In this context the bosons act upon weak isospin doublets that are formed by a neutrino and corresponding charged lepton or an up-type quark and down-type quark pair by changing one particle of the doublet into the other. Since the mass eigenstates of quarks differ from their weak eigenstates and the latter can be expressed through a superposition of the former, any up-type quark can interact with any down-type quark through the charged weak current, which makes flavour changes possible. The weak eigenstates for down-type quarks and in extension also the strength of this interaction between different kinds of quarks is given by the CKM matrix [11, 12],

$$\begin{pmatrix} d' \\ c' \\ b' \end{pmatrix} = \begin{pmatrix} V_{ud} & V_{uc} & V_{ub} \\ V_{sd} & V_{sc} & V_{sb} \\ V_{td} & V_{tc} & V_{tb} \end{pmatrix} \cdot \begin{pmatrix} d \\ c \\ b \end{pmatrix}. \tag{2.1}$$

This consideration does not apply to leptons since a designated neutrino i.e. electron neutrino already is the weak eigenstate.

The Z^0 boson is best understood within the context of electroweak unification given by the non-Abelian symmetry group $U(1)_Y \times SU(2)_L$ [6, 9, 10], as it is observed to couple to both left-handed and right-handed fermions, while the uncharged weak isospin boson W^0 obtained from $SU(2)_L$ only couples to left-handed fermions. A new quantum number called weak hypercharge $Y = 2(Q - I_3)$ is introduced as the symmetry of $U(1)_Y$ to which its neutral gauge boson B^0 couples. The Z^0 and γ bosons are then obtained through a rotation of the uncharged boson state containing B^0 and W^0 about the weak mixing

angle θ_W. The Z^0 boson mediates a neutral current between particles that is not able to change electric charge or flavour quantum numbers. Even though the Z^0 couples to fermions of any handedness, the coupling to left-handed fermions is preferred, owing to the contribution of the W^0 boson. Unlike other gauge bosons, the W and Z^0 bosons are massive particles, that obtain their mass through spontaneous symmetry breaking via the Higgs-Mechanism [13].

The Strong Interaction

The theory describing the strong interaction is called Quantum Chromodynamics (QCD) and is based on the local gauge symmetry of $SU(3)_C$, giving rise to eight massless gauge bosons named gluons [6, 14, 15]. Gluons couple to particles that carry a colour charge denoted as red, green, or blue. Since $SU(3)_C$ is non-Abelian, gluons are able to self-interact, as they carry a combination of colour and anticolour charge themselves. Leptons do not carry a colour charge, therefore the only fermions that interact via the strong interaction are quarks.

A fundamental concept of QCD is the concept of colour confinement [16], which states that no free particles with non-zero colour charge can exist. This leads to the formation of colourless objects called hadrons of which there are two types: mesons made of a quark and antiquark with corresponding colour/anticolour and baryons/antibaryons made of three quarks where every quark has a different colour/anticolour or five quarks where the additional two quarks have the same characteristics as in a meson. This concept can be understood by looking at the potential of the strong interactions given by [17],

$$V(r) = -\frac{4}{3}\frac{\alpha_s}{r} + \kappa r \,, \tag{2.2}$$

where r is the spatial distance between quarks and $\kappa \sim 1\,\mathrm{GeV/fm}$ is the constant factor of the linear term. The energy stored in the field increases with the distance between quarks until it is energetically favourable to create a new pair of quarks, which eventually leads to the formation of particle cascades consisting of colourless hadrons. This process of high energy quarks producing high multiplicity cascades is known as hadronisation. Quantum Chromodynamics furthermore possesses a property called asymptotic freedom, which causes the coupling strength of the strong interaction to decrease asymptotically with increasing energy scale [14, 18]. The coupling constant α_s becomes small enough at high energies to allow a perturbative approach to QCD.
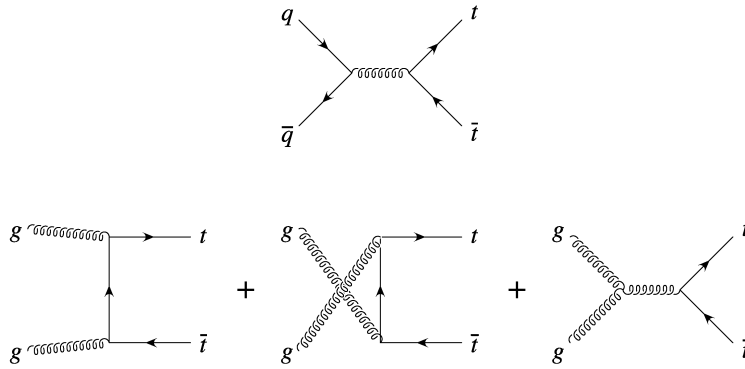
Abb. 2.2: Feynman diagrams for $t\bar{t}$ production modes.

2.2 The Top Quark

The existence of the top quark was predicted in 1973 by M. Kobayashi and T. Maskawa as the up-type quark of the third fermion generation, making it the weak isospin partner of the bottom quark [19]. Accordingly it has an electric charge of $Q = +\frac{2}{3}$e. With a mass of $m_t = (172.69 \pm 0.30)\,\text{GeV}$ [20] it is also the most massive elementary particle known and exhibits the strongest coupling to the Higgs field. It was finally discovered in 1995 by the CDF and DØ Collaborations at the TEVATRON [21, 22].

With an expected lifetime of $\tau = 5 \cdot 10^{-25}\,\text{s}$, it decays before it can hadronize, creating the unique opportunity to investigate bare quark states, since its properties are passed on to the decay products [20]. For instance, it decays before the spin polarization in top quark pairs can be decorrelated through the strong interaction, making it suitable for the investigation of spin entanglement in quarks.

To study spin entanglement of top quarks at hadron colliders, $t\bar{t}$ pairs first have to be produced from the collision. At proton-antiproton colliders such as the TEVATRON, the dominant production mode is quark-antiquark annihilation (see Fig. 2.2) while at proton-proton colliders such as the LHC the $t\bar{t}$ production is dominated by gluon-gluon fusion (90%), for which the leading-order Feynman diagrams are shown in Figure 2.2 [20].

2.2.1 Top Quark Decay

The top quark decays weakly into a W boson and a down-type quark. The specific decay rates are proportional to their respective CKM matrix elements. As a result of $|V_{tb}| \approx 1$, the top decay is dominated by bW, while the cross-generational decays into a down or strange quark are higly suppressed [20].
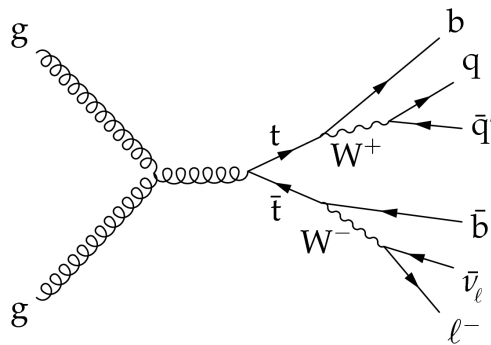
Abb. 2.3: Feynman diagram of the semileptonic decay of a $t\bar{t}$ produced via gluon-gluon fusion.

The W boson further decays hadronically into a quark-antiquark pair ($q\bar{q}$) or leptonically into a charged lepton and lepton neutrino pair. The hadronic decay is the dominant mode with a branching ratio of $(66.5\pm0.5)\%$ while the remaining $\sim 1/3$ decay leptonically into one of the three lepton pairs at the same rate because of lepton universality [20]. There are three possible final state configurations of the $t\bar{t}$ decay in which two W bosons are produced: fully-hadronic with a branching ratio of 44.2%, dileptonic with 11.2% and semi-leptonic with 44.6% in which case one of the two W decays hadronically and the other leptonically. The semileptonic decay channel, which is used for the analysis in this thesis, has the highest share of the $t\bar{t}$ final state and therefore provides a strong signal in a detector, while the easily detected lepton signature also assures a good distinction between desired signal and the other decay modes. The leading-order Feynman diagram for this decay channel is shown in Figure 2.3.

2.2.2 Quantum Entanglement

In quantum mechanics, entanglement is a property of the state of a composite quantum system where a state is said to be entangled if it cannot be separated into the states of the subsystems i.e. it is not possible to assign a well defined state to each of the subsystems. Quantum states are generally described by a density matrix ρ, a semi positive-definite, Hermitian operator with unit trace acting on the Hilbert space H of the system. In the case of a bipartite system $H_A \otimes H_B$ the composite state is separable, and as such not entangled, if it can be expressed as,

$$\rho = \sum_k w_k \rho_k^A \otimes \rho_k^B,\tag{2.3}$$

where w_k are nonnegative probabilites and $\rho_k^{A/B}$ are states in the subsystems H_A and H_B.

In the case of a bipartite composite system with two-dimensional subsystems, a sufficient criterion for the entanglement is given by the Peres-Horodecki criterion. It states that ρ is separable if and only if the eigenvalues of the partially transposed density matrix with respect to the second subsystem are non-negative [23, 24].

Since top quarks are spin-$\frac{1}{2}$ particles, the component of their spin along a given direction can take on only two different values. As such, a top quark fits the definition of a two qubit system. The density matrix for a two qubit system is given by,

$$\rho = \frac{I_4 + \sum_i (B_i^+ \sigma^i \otimes I_2 + B_i^- I_2 \otimes \sigma^i) + \sum_{i,j} C_{i,j} \sigma^i \otimes \sigma^j}{4}, \tag{2.4}$$

where $\sigma^i, i, j = 1, 2, 3$ are the Pauli matrices and I_n are the $n \times n$ identity matrices. The spin polarisation is described by the vectors $\mathbf{B}^\pm$, $B_i^+ = \langle \sigma^i \otimes I_2 \rangle$, $B_i^- = \langle I_2 \otimes \sigma^i \rangle$, while $\mathbf{C}$ denotes the spin correlation matrix, $C_{i,j} = \langle \sigma^i \otimes \sigma^j \rangle$. By applying the Peres-Horodecki criterion on the qubit state, it can then be shown that,

$$\text{tr}[\mathbf{C}] < -1, \tag{2.5}$$

is a sufficient criterion to demonstrate the entanglement of a state [25].

2.2.3 Spin Observable

A top quark pair produced through gluon-gluon fusion near treshhold, i.e. with an invariant mass close to two times the nominal top mass ($m_{t\bar{t}} \approx 345\,\text{GeV}$), is produced in an unpolarized spin singlet state in which the top spins are entangled [20]. As previously mentioned, the spin information of the top pair is preserved in the angular distribution of its decay products. This angular distribution is correlated to the top spin axis in the following way [26, 27],

$$\frac{1}{\Gamma}\frac{d\Gamma}{d\cos\vartheta_i} = \frac{1}{2}(1 + \alpha_i \cos\vartheta_i), \tag{2.6}$$

where ϑ is the angle between the momentum direction of the i-th decay product and the top spin axis. The factor α_i is called the spin analyzing power of the decay product. It indicates how strongly the direction of flight is correlated to the top spin. Table 2.1 lists the values for the relevant top quark decay products. In antitop decay, the signs of these values are flipped. In the semileptonic channel, charged leptons as well as down and strange quarks clearly exhibit the strongest correlation. Since the W decays that produce a strange quark also almost always produce a charm quark due to CKM suppression, it is possible to identify the strange quark by pairing it with a charm quark which in turn can

Tab. 2.1: Spin analysing power for decay products in semileptonic $t\bar{t}$ decay [28]

	$\bar{u}/\bar{c}$	$\bar{d}/\bar{s}$	$\bar{b}$	l^+	W^+
α (LO)	0.32	1	0.41	1	0.41
α (NLO)	0.31	0.93	0.39	0.998	0.39

be identified through a *c*-tagging approach. For this reason the two spin analyzers that will be used in this analysis are the charged lepton and either a strange or down quark, since it is not possible to experimentally distinuish these two quarks. This does not pose a problem to the analysis as both quarks have the same spin analyzing power. Thus only bottom quarks are vetoed.

To access the entanglement signature of the $t\bar{t}$ system it is possible to define an angular distribution using the opening angle φ between the momentum directions of these two spin analyzers $\hat{l}, \hat{s}$ in their respective parent top/antitop rest frame [25, 29], $\cos\varphi = \hat{l} \cdot \hat{s}$,

$$\frac{1}{\sigma}\frac{d\sigma}{d\cos\varphi} = \frac{1}{2}(1 - D\cos\varphi). \tag{2.7}$$

The value for D can be directly extracted from the above distribution via,

$$D = -3 \cdot \langle\cos\varphi\rangle. \tag{2.8}$$

It is connected to the trace of the spin correlation matrix via $D = \text{tr}[\mathbf{C}]/3$ [25]. By applying the Perez-Horodecki criterion from before, the obervable $\cos\varphi$ becomes a direct, experimentally accessible measure for spin entanglement in the $t\bar{t}$ system. The criterion, that has to be fullfilled for entanglement to be present, is then translated to [25],

$$D < -\frac{1}{3}. \tag{2.9}$$

2.3 Evolution of Hadronic Scattering Events

The high-energy particle collisions and subsequent scattering processes taking place at particle accelerators produce complex event topologies. Therefore, the particles that are measured within the detector usually do not coincide with the elementary particles originating from the primary hard scattering. To still be able to test theory predictions against actual detector data, physicists thus have to simulate this evolution of the primary hard scattering process based on theory and phenomenology. This task is achieved in computational particle physics using tools called Monte Carlo Event Generators that simulate the evolution of the high-multiplicity particle showers from the hard scattering process

in high-energy particle collisions based on theory and phenomenology. Previous studies have shown that the predictions of the entanglement observable $\cos\varphi$ from Eq. 2.8 depend in particular on the parton shower algorithm employed by the generator program. This thesis therefore aims to examine the systematic uncertainties in the entanglement observable that emerge from parton shower modelling using the two mainstream Monte Carlo Generators PYTHIA and HERWIG. This section will provide a brief overview of the physics behind the parton showers and the methods used in their simulation in computational particle physics.

2.3.1 Parton Model & Hard Scattering

The parton model is a theoretical framework in particle physics that describes the internal structure of hadrons in terms of their fundamental constituents. These constituents, either quarks or gluons, are called partons. At high energies, the partons within a hadron can be approximated as nearly free and point-like entities due to the weakening strong interaction at short distances as a consequence of asymptotic freedom. As such, the parton model provides a way to calculate the interactions of particles in high-energy collisions using perturbation therory in terms of individual partons rather than the composite hadron itself [30].

To achieve this, the parton model introduces the concept of parton distribution functions $f(x, Q^2)$ (PDFs) [31]. PDFs describe the probability of finding a parton carrying a specific momentum fraction x of the hadron's total momentum at the momentum transfer square Q^2 of the scattering process. The PDFs encompass the non-perturbative aspects of QCD, representing the long-distance physics of quark and gluon confinement within hadrons. The parton densities do not directly emerge from theory calculations but can be determined through experimental data from different scattering processes, since they are intrinsic properties of a specific hadron and therefore do not depend on the specific type of interaction.

The concept of factorisation allows for a calculation of the overall cross-section of a scattering process through the separation of the long-distance physics of the hadron structure from the short-distance physics of the parton interactions, with the short-distance physics being described by perturbatively calculable partonic cross-sections. According to the factorisation theorem, the cross-section for a hadronic hard scattering process, i.e. scattering with high momentum transfers or large momentum transfers Q^2, $h_A + h_B \to X_1 + ... + X_n$

has the form [32, 33]:

$$\sigma = \sum_{a,b} \int_0^1 dx_A \int_0^1 dx_B f_A^a(x_A, Q^2) f_B^b(x_B, Q^2) \hat{\sigma}_{ab}(x_A x_B s, Q^2), \tag{2.10}$$

where $\hat{\sigma}_{ab}$ is the partonic cross-section for partons a and b, x_A and x_B are their longitudinal momentum fractions with respect to their hadron and s is the squared centre-of-mass energy of the incoming hadrons. The partonic cross-section can be calculated via the matrix element for the specific parton interaction obtained by perturbation theory.

2.3.2 Parton Showers

Following the initial hard process, the scattered coloured partons emit QCD radiation in the form of gluons. These gluons subsequently either split into a quark-antiquark pair or emit further gluons as they themselves carry colour charges. This branching process of high-energy partons radiating lower energetic partons leads to the formation of a PAR-TON SHOWER, continuing for as long as the energy is high enough for more emissions to occur. The parton shower typically includes next-to-leading order (NLO) or even NN-LO corrections to the calculation of the hard scattering cross-section. It can generally be approximated by considering the contributions from collinear branching and soft-gluon emission. The cross-section under a collinear parton splitting $a \rightarrow b+c$ evolves via [34, 35]

$$d\sigma_{n+1} = d\sigma_n \frac{d\theta^2}{\theta^2} dz \frac{\alpha_s}{2\pi} P_{ab}(z), \tag{2.11}$$

where θ is the opening angle of the parton splitting and P_{ab} is the so-called splitting function, which describes the probability distribution of parton b carrying the energy fraction z of parton a. The parton shower develops with decreasing hardness of interactions. Using the virtual momentum-squared q^2 (virtuality) of partons in a branching as a measure for the hardness allows for the introduction of a cut-off scale Q_0^2. If a branching drops below this cut-off, it remains unresolved leading to the termination of the shower. The probability of a parton a evolving from virtuality q_1 to q_2 without any resolvable parton emission is given by the Sudakov form factor $\Delta_a(q_1, q_2)$ [36],

$$\Delta_a(q_1, q_2) = \exp\left\{ -\int_{q_1^2}^{q_2^2} \frac{dq^2}{q^2} \frac{\alpha_s}{2\pi} \int_{Q_0^2/q^2}^{1-Q_0^2/q^2} dz P_{ab}(z) \right\}. \tag{2.12}$$

This form factor can be used in parton shower algorithms to simulate the shower evolution by utilizing the Monte Carlo (MC) method, a technique for numerical integration using random numbers. The parton shower develops from initial scale q_1 by solving the equation

$\Delta_a(q_1, q_2) = R$ for q_2, where R is a random number uniformely distributed on the interval $[0, 1]$. If $q_2^2 > Q_0^2$, the parton splits and the process is repeated for the new partons at momentum scale q_2^2. If $q_2^2 < Q_0^2$, the branching remains unresolved. At each step, the energy fraction z is determined via the Monte Carlo method applied to the partons splitting function [34, 35].

2.3.3 Hadronisation

After the hardness of parton interactions falls below the aforementioned cut-off scale and the shower terminates, the coloured partons arrange themselves to form colour-neutral hadrons via a process called hadronisation. Hadronisation is a non-perturbative effect of the low momentum transfer, long-distance regime of QCD that cannot be calculated directly, as no exact hadronisation theory exists. Instead, Monte Carlo simulations based on phenomenological models are used to describe the hadronisation process. There are two approximate but successful models for hadronisation with one each being used by the Monte Carlo Shower Generators studied in this thesis.

Lund String Model: In the Lund String Model, the partons are connected by colour strings. Colour string form between particles carrying a colour charge and represent the field of the strong interaction between them. As the partons move apart, the energy stored in the string increases until it eventually breaks up into a pair of smaller strings via the creation of a new quark-antiquark pair. These newly created quarks and antiquarks can then either participate in further string breaking if their energy is high enough or combine to form mesons or baryons. This fragmentation process continues until each colour charge is bound within colour-neutral hadrons [35, 37].

Cluster Model: In the Cluster Model, the coloured partons produced in the collision form colour-neutral clusters of quarks and gluons whose momentum is given by the total momentum of the constituent partons. After the inital decay of leftover gluons into quark-antiquark pairs, only quarks and diquarks remain in the clusters. Diquarks describe an energetically favourable assembly of two quarks with a non-zero colour charge that can recombine with another quark to form a baryon. The clusters finally decay into colour-neutral hadrons with heavy clusters first splitting into lighter clusters in a process called cluster fission [34, 38].

The hadrons formed from partons after fragmentation and hadronisation typically include a large fraction of unstable particles, such as excited hadronic states. These unstable

hadrons decay shortly after their formation before ever reaching a potential detector until only relatively stable particles like protons, neutrons, pions, or kaons remain, which could be detected in a detector experiment. These hadron decays consequently have to be included in the simulation of particle collision events. For this analysis specifically it is essential for spin correlations to be taken into account in the modelling of hadron decays.

2.4 Jets

As a consequence of the conservation of energy and momentum, the stable hadrons that emerge from the collision are emitted as collimated bunches in a cone-like pattern with large and roughly parallel longitudinal momenta. These particle sprays, called JETS, are observable objects that can be detected and measured in a particle detector. Jets therefore play a crucial role in experimental particle physics, as they connect the experimental measurements to theory predictions, which are originally formulated in terms of partons. Jets are characterized by several properties [34, 35, 39, 40]:

- **Collimation:** Jets are collimated sprays of particles. This collimation starts from the initial momentum direction of the parton that initiates the jet and is maintained through subsequent parton showering, fragmentation, and hadronization.

- **Particle Multiplicity:** During the evolution of the scattering event, partons undergo branching and fragmentation, resulting in the emission of a cascade of lower-energy particles, which leads to a high multiplicity of hadrons within a jet.

- **Structure and Substructure:** Jets can have substructures such as subclusters of energetic particles. These substructures can be used to obtain information about the parton that initiated the jet, or to distinguish a signal jet from background jets, i.e. jets originating from gluons.

- **Energy and Momentum:** Jets possess a set amount of energy and momentum, which is distributed among its constituent particles. These quantities can be measured experimentally, providing insights into the initial parton's properties, such as energy and momentum or even its original particle identity.

Jet algorithms are employed in the simulation of detector events or their reconstruction from data. The two major requirements for such an algorithm are infrared and collinear safety. An observable is infrared safe if it does not depend on the low energy physics processes. In terms of jet reconstruction this translates to the algorithms ability to identify and count jets not being affected by soft particle emissions. The requirement for collinear

Tab. 2.2: Parametrisation of sequential clustering algorithms according to Eq. 2.13

Algorithm	n
k_T	2
Cambridge-Aachen	0
Anti-k_T	-2

safety means that the jet identification should not be sensitive to collinear splittings of particles in the shower. Jet algorithms can generally be separated into cone algorithms, that typically do not satisfy the above requirements with the exception of SISCone [41], and sequential clustering algorithms such as the k_T [42], anti-k_T [43], or Cambridge/Aachen [44] algorithms, that are collinear and infrared safe by construction [45]. These clustering algorithms construct the jet hirarchically, ordered by their momentum k_T transverse to the beam direction z in a collider experiment. For this purpose, they introduce the measures,

$$d_{ij} = \min(k_{T,i}^n, k_{T,j}^n)\frac{\Delta R_{ij}^2}{R^2}, \tag{2.13}$$

$$d_{iB} = k_{T,i}^n, \tag{2.14}$$

where d_{ij} is the distance between entities i and j (particles, jets) and d_{iB} between entity i and the beam B, R is a free parameter describing the characteristic cone radius and $\Delta R_{ij}^2 = (y_i - y_j)^2 + (\phi_i - \phi_j)^2$ represents the distance between the four-momenta of two entities in (η, ϕ) space [45]. These coordinates denote the particle's rapidity $y = \frac{1}{2}\ln\left(\frac{E+p_z}{E-p_z}\right)$ and azimuthal angle ϕ. They are introduced with more detail in Section 3.2. The parameter n determines the specific type of algorithm as shown in Table 2.2. At each step of the clustering algorithm, the smallest distance in the set of all $d_{i,j}$ and $d_{i,B}$ is identified. If this smallest distance is d_{ij}, the two entities are merged into one and their four-momenta are combined. If the smallest distance is d_{iB}, the entity is counted as a final jet and is removed from the list of entities. Its four-momentum is merged with the beam. After each step, the distances are recalculated for the remaining entities until either all four-momenta are merged with the beam (inclusive algorithm) or a fixed distance cut-off measure d_{cut} is reached (exclusive algorithm).

3 Experimental Setup

High-energy particle colliders and particle detectors are used to artificially create and study the elementary particles of the Standard Model.

3.1 The Large Hadron Collider

The LARGE HADRON COLLIDER (LHC) is a 27 km long particle accelerator at the European Organisation for Nuclear Research (CERN) in Geneva, Switzerland. It is both the largest and most powerful accelerator in the world in terms of beam energy. The LHC is mainly operated as a proton-proton (pp) collider but is also used to collide heavy-ions such as lead or xenon. Particles are first accelerated through a chain of smaller accelerators before they are injected into the main accelerator. The LHC is a synchrotron-type accelerator utilizing oszillating electric fields for particle acceleration along straight cavities while superconducting magnets that are synchronized to the particles kinetic energy focus and bend the particle beam along the circular orbit [46]. The beam collisions at the LHC do not occur between single particles but instead between so called bunches, each consisting of up to 10^{11} protons in *pp* collisions. During its first fully operational run from 2010 to 2013 the colliding proton beams each reached a beam energy of 3.5 to 4 TeV while the second run from 2015 to 2018 already reached a beam energy of 6.5 TeV with a resulting centre-of-mass energy of 13 TeV. The beam energy of the third run, which started in the summer of 2022 and is currently ongoing, was further improved to 6.8 TeV. The planned High Luminosity LHC update is expected to further raise the beam energy to 7 TeV and increase the integrated luminosity by a factor of 10 [47].

3.2 The ATLAS Detector

The ATLAS detector [48], which is presented in Fig. 3.2, is the largest particle detector at a high-energy collider in the world. Collisions between proton bunches at ATLAS occur every 25 ns with around 1000 decay particles flying into all directions, most of which close to the original beam axis [48]. These directions are defined using the ATLAS COORDINATE SYSTEM, which places the nominal interaction point in its origin as shown in Fig. 3.1.
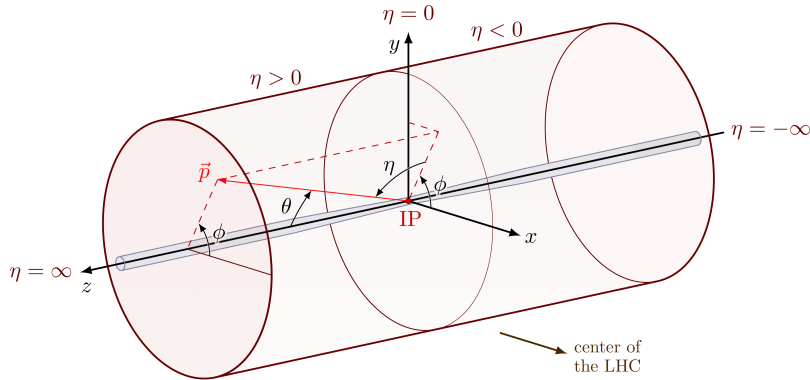
Abb. 3.1: Schematic of the ATLAS Coordinate System.

The z-axis is defined along the beam direction and the $x - y$ plane is defined to be the plane transverse to the beam direction with the x-axis pointing towards the center of the accelerator ring. The angle at which a particle flies out from the collision point is then determined using the polar angle θ to the x-axis and the azimuthal angle ϕ to the beam axis. The azimuthal angle is further mapped onto a quanitity called pseudorapidity, defined by,

$$\eta = -\ln\left[\tan(\tfrac{\theta}{2})\right], \tag{3.1}$$

as particle emission is roughly constant over an intervall in pseudorapidity and differences in pseudorapidity are Lorentz invariant under boosts along the longitudinal axis. The pseudorapidity η is the high-energy limit $E \approx p$ of the previously introduced rapidity y. The detectors cylindrical structure can generally be separated into four different parts that are layered around the beam pipe: the INNER DETECTOR (ID), the CALORIMETER SYSTEM and the MUON and MAGNET SYSTEMS. Each detection layer is used to measure different properties of specific particles. A particle's identity and origin can then be reconstructed by using the signatures left in the different layers as indicated in Figure 3.3.

The Inner Detector

The INNER DETECTOR is itself made out of three different layers that cover $|\eta| < 2.5$. The innermost hybrid pixel detectors and microstrip semiconductor detectors made out of silicon are used to track the trajectory of decay products right outside the collision point to reconstruct the vertex they originated from. Beyond that lies the TRANSITION RADIATION TRACKER made of up to 73 layers of straw tubes interleaved with fibres which is also used for tracking as well as for electron/pion identification. The entire ID is further permeated by in a $2\,\mathrm{T}$ solenoidal magentic field. The trajectories of electrically charged particles that pass through this field are bent as a consequence of the Lorentz
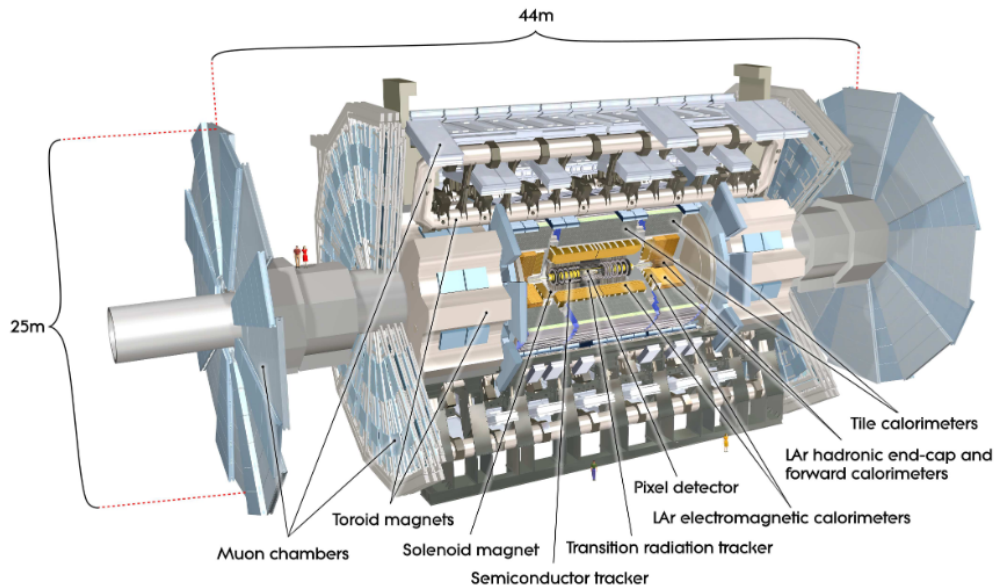
Abb. 3.2: Overview of the ATLAS detector at and its components, © CERN [48].

force. It is then possible to reconstruct their transverse momentum p_T through the extent of the curvature. Particles like neutrons that do not interact electromagnetically do not leave a signature in the tracking detectors of the ID [48].

The Calorimeter System

Outside the ID lies the CALORIMETER SYSTEM of ATLAS in which particles are stopped to measure their energy. It covers a range of $|\eta| < 4.9$ and consists of an electromagnetic calorimeter (ECal) on the inside and a hadronic calorimeter (HCal) on the outside. Both of which are sampling calorimeters that use a passive medium to induce a particle shower and an active medium to generate detectable signals [48].

The Electromagnetic Calorimeter consists of a barrel part ($|\eta| < 1.475$) and two end-caps ($1.375 < |\eta| < 3.2$). It measures particles that interact electromagnetically using a lead absorber to induce an electromagnetic shower. Liquid Argon (LAr) is used as the active medium. It is also prefaced by a LAr pre-sampler in the region $|\eta| < 1.8$ to detect and compensate for showers that had already started in the ID. Electrons and photons deposit their entire energy in the ECal. Heavier particles such as muons and charged hadrons are not stopped in the electromagnetic calorimeter [48].

The Hadronic Calorimeter is used to measure the energy of particles that are subject to the strong interaction by inducing hadronic showers. For neutral hadrons this is the only way to measure their energy. The HCal of ATLAS is divided into three parts. A tile calorimeter surrounds the ECal barrel and end-caps covering a range of $|\eta| < 1.7$. It uses steel as a passive medium and scintillating tiles to generate a signal. Behind the ECal
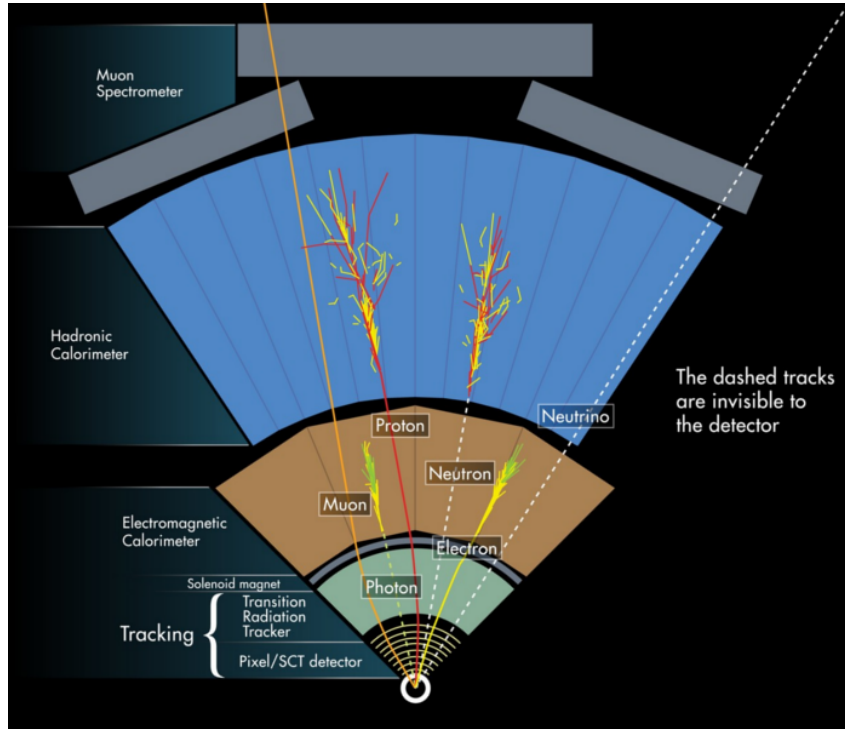
Abb. 3.3: Overview of the concentric detection layers in ATLAS and their interaction with different particles, © CERN.

end-caps lies the hadronic end-cap calorimeter ($1.5 < |\eta| < 3.2$), which uses LAr as the active medium and copper plates as its passive medium. The hadronic barrel and end-cap calorimeters are larger than the electromagnetic ones since the hadronic interaction length is longer relative to the radiation length but their measurements are less precise compared to the electromagnetic calorimeter [48].

Finally a LAr forward calorimeter covers the range of $3.1 < |\eta| < 4.9$ between the beam pipe and end-cap calorimeters. It consists of a copper module that is optimized for electromagnetic measurements on the inside and a tungsten module optimized for hadronic measurements on the outside [48].

The Muon System

The MUON SYSTEM is the outermost and by far the largest part of the ATLAS detector covering a range of $|\eta| < 2.7$. It is specifically designed to detect muons since most other particles except neutrinos are stopped within the calorimeters. The muon tracks are bent in the toroidal magnetic field of three superconducting magnets in the barrel ($1.4 < |\eta|$) or the two toroid end-cap magnets ($1.6 < |\eta| < 2.7$) allowing for the measurement of the muons momentum. In the transition region ($1.4 < |\eta| < 1.6$) tracks are bent by a

combination of the barrel and end-cap magnets.

The muon spectrometer can be divided into four different sub-systems. MONITORED DRIFT TUBES (MDT, $|\eta| < 2.7$) and CATHODE STRIP CHAMBERS (CSC, $2.0<|\eta|<2.7$) are used for high precision tracking and momentum measurement while RESISTIVE PLATE CHAMBERS (RPC, $|\eta| < 1.05$) and THIN GAP CHAMBERS (TGC, $1.05 < |\eta| < 2.7$) provide the second spatial coordinate complementing the MDT measurements since MDTs are only capable of measuring the projection of the particles trajectory perpendicular to to the drift tubes and can not determine their position along the tubes. The RPC and TGC also form the MUON TRIGGER SYSTEM which functions as a hardware level trigger on the muon momentum. Structurally, the muon spectrometer is divided into a barrel part and an end-cap part. The barrel consists of three concentric layers of MDTs around the beam axis that are further interfaced with RPCs on the outside. Different distances between RPC layers allow for high- as well as low-p_t triggering. The end-caps are equally made up of three layers with the chambers being installed in planes perpendicular to the beam. The innermost tracking layer is equipped with CDCs as the incidency in the $|\eta| > 2$ region of the first end-cap layer exceeds the safe operating limit of MDTs. Beyond the end-cap magnets lie two layers of MDTs with the outermost layer being the iconic shields of the ATLAS detector. Between the MDTs, three layers of TGCs are installed with the same uses as the RPC layers in the barrel [48].

The Trigger System

ATLAS detects 600 million inelastic events per second which corresponds to an enormous amount of data that is impossible to store. Triggers are therefore implemented to filter out only those events that are interesting for actual analysis. Detector-level hardware trigger (L1) like the muon trigger cut down the data signal to $75\,\mathrm{kHz}$ and define Regions of Interest (RoI) that are examined more precisely using software algorithms. The second level trigger (L2) processes the RoI data that was accepted by the L1 trigger and further reduces the signal to $3.5\,\mathrm{kHz}$. Finally, computation heavy event filters reduce the signal down to $1000\,\mathrm{Hz}$. The L2 trigger and event filter together form the High Level Trigger (HLT) that runs on external computation hardware. Data that passes the HLT is then finally stored [48].

4 Event Generation

Event generation is an essential tool for simulations in experimental particle physics. This chapter briefly discusses the basics of event generation and introduces the two Monte Carlo generators PYTHIA and HERWIG, whose parton shower modelling effects on the spin observable will be examined in this thesis.

4.1 Overview

In particle physics, the term "*event*" refers to a specific scattering process between particles colliding within a detector. Each event provides information about the particles involved, including their properties (e.g. their type, energy, momentum, and charge), and the characteristics of their interaction. As such, events serve as the basis for studying the physics of particle collisions. In particle detectors, the full information about an event is not directly available from detector measurements. Instead, the events first have to be reconstructed from detector data. To test the predictions made by theoretical models, comparable events need to be calculated from the relevant theory. Since the interactions in such high-energy scattering events are vastly complex, a direct calculation is generally not possible. Therefore, the events have to be simulated using approximations and phenomenological methods. The computational programs used for this purpose are called Monte Carlo Event Generators. As the name suggests, these simulations rely on the method of Monte Carlo integration. Event Generators use sophisticated algorithms to simulate the different stages of the scattering process as shown in Fig. 4.1. These stages include a hard process, typically at LO or NLO[1] of perturbative calculations, parton showering, and Beam Remnants [49]. They succesfully employ phenomenological models to simulate any subsequent hadronisation as well as the underlying event including Multiple Particle Interactions, i.e. secondary hard processes involving partons that did not participate in the primary hard process. An event can fundamentally be described on three different

---

[1]The parton level hard scattering cross-sections are calculable in perturbative QCD as a series expansion in α_S. The leading-order (LO) term corresponds to the α_S^0 contribution while the next-to-leading-order ($\mathrm{N}^k\mathrm{LO}$) corrections correspond to the α_S^k contributions
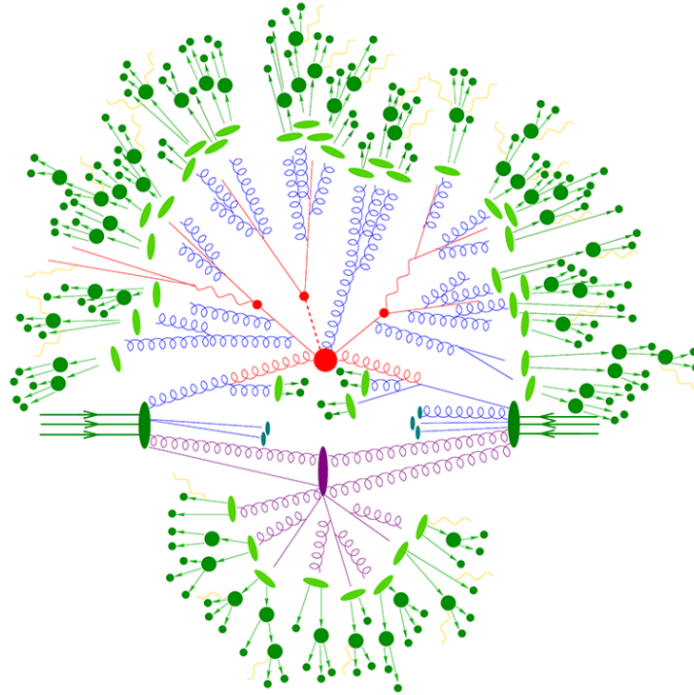
Abb. 4.1: Schematic of a hadronic scattering event as simulated by a Monte Carlo Event Generator. The dark-green arrows on the left and right represent the incoming hadrons characterized by their PDFs. The red part represents the hard scattering process and its resonant decays. The wiggly blue lines indicate a parton shower and the light-green blobs the subsequent hadronisation. The dark-green blobs signal hadron decays with the yellow lines showing the emission of soft photon radiation. The purple parts on the bottom indicate a Multiple Partonic Interaction. The straight blue lines and turquoise dots show the Beam Remnants, that did not interact.

stages of analysis:

Parton Level: An event on parton-level contains full information on the particles involved in the scattering process, including their properties, identities, decay products, and dynamics of their interactions, which is why the parton level is sometimes also called truth-level. The physics objects in parton-level events include the original partons and other elementary particles emerging from the scattering events. Therefore, parton-level events are unaffected by the specifics of Shower Monte Carlo simulation. Since the theory of particle interactions is formulated in terms of partons, theory predictions have to be evaluated on parton-level, which is why the parton-level information has to be reconstructed from events, that are not available on parton-level, such as events from actual detector data.

Particle Level: A particle-level events refers to the final state of a scattering process after hadronisation has taken place and jets have been formed. The physics objects of a particle-level event therefore do not include the original partons but the jets that are simulated using Shower MC programs along with other stable scattering products, e.g. electrons. As such, the parton-level encompasses the phenomenology of particle collisions, thereby reducing the sensitivity to theory. The final state particles of a particle-level event can interact with a possible detector such as the ATLAS experiment.

Reco Level: On reco-level or detector-level, an event is characterized by its reconstruction from the measurable signatures left in a detector by its particle-level final state, such as energy, momentum, and charge. Therefore, unlike the previous two levels, reco-level analysis is immediately available for both Monte Carlo and data events, allowing for the direct comparison of the two. Inefficiencies in a detector, such as gaps between detector elements, limited resolution, detector acceptance or simply the complexity of a particle's interaction with matter limit the information about an event, which subsequently leads to imperfections in the reconstruction. If the detector was 100% efficient, reco and particle-level would be identical. To simulate these detector effects in Monte Carlo generated events a detector simulation is employed.

4.2 Production of Event Samples

The $t\bar{t}$ samples in this analysis were produced under conditions of LHC Run-II in 2018 using the Monte Carlo Event Generators PYTHIA and HERWIG for the parton shower (PS) merged with POWHEG [49]. PYTHIA and HERWIG are both classified as General-Purpose Event Generators, that are able to simulate the entirety of a common QCD event at particle colliders [34, 35]. POWHEG is used to achieve NLO accuracy in the perturbative calculations. The output of these NLO+PS simulations are particle-level event samples as described above. They also produce parton-level samples, that are not affected by the specifics of the parton shower program, which makes it possible to directly compare the effects of using different parton shower generators. The reco-level sample is obtained by applying an ATLAS detector simulation to the particle-level events using GEANT4 [50]. GEANT4 recreates the geometry of ATLAS described in Section 3.2 and simulates the interaction of particles and radiation with its detector elements. There are two sets of HERWIG and PYTHIA samples used in the analysis that were produced in a different manner. One set was produced using the full detector simulation, while the other set was produced using a fast simulation scheme [51]. The purpose of fast simulation is to reduce

the time and computational resources required for the simulation, as one sample can easily consist of hundreds of millions of events, making the simulation very time-consuming. This can be achieved through the parameterisation and subsequent parameter smearing of the particles track, the detectors complex geometry, as well as the particles interaction with the sensitive detector material.

4.2.1 PYTHIA

PYTHIA is a standard Monte Carlo program for the generation of events in high-energy particle collisions with a centre-of-mass energy greater than $10\,\text{GeV}$ [35]. It uses a set of physics models to simulate the particles and interactions of the Standard Model but also includes models of physics beyond the SM such as Supersymmetry or Dark Matter. Below the $10\,\text{GeV}$ limit, some approximations within these models start to break down, leading to inaccurate predictions, especially in hadron-hadron cross-section calculations [52].

PYTHIA is capable of simulating the entire evolution of a hard scattering into a high multiplicity final state, covering many hard-QCD and electroweak processes under the subclasses of $2 \to 1$, $2 \to 2$, or $2 \to 3$, such as scattering of gluons and quarks, boson (pair) productions or photon-parton scattering. Perturbatory calculations in PYTHIA are generally formulated at leading order with some next-to-leading order corrections being included. The entire perturbatory process including intial and final state parton showers evolves according to a sequence of decreasing p_T-related hardness (virtuality) [53]. The parton shower algorithm is based on colour-anticolour dipole splittings and relies on the Sudakov form factor of Eq. 2.12 [35]. To address the colour coherence of parton emission in the soft shower stage, an angular-ordering requirement is introduced to the shower. The effects of spin correlation are taken into account, when calculating the matrix element for a given hard process or decay. Hadronisation in PYTHIA is simulated using the Lund-String model as discussed in Section 2.3.3. The phenomenological character of this model requires the input of external parameters, which have to be determined through comparisons to measured data. PYTHIA uses the FASTJET package to construct jets. This package includes a set of infrared and collinear safe clustering and cone algorithms [54].

The event samples in this thesis were generated using the PYTHIA 8.2 version. This version is the second main release of PYTHIA that is coded in C++, with earlier versions originally being written in Fortran. As of this version, most functionalities of the previous Fortran version, such as $2 \to 3$ QCD-processes, which play a particularly important role in parton showers, as well as top pair production and full implementation of spin correlation in particle production and decays among other features are included [52].

4.2.2 HERWIG

HERWIG is another standard event generator, that is able to simulate the entire evolution process of an event as illustrated in Fig. 4.1 [34]. HERWIG is fundamentally a leading-order generator with some NLO calculations being included. Next to the dipole-style parton showers, shower simulations of HERWIG are based on the coherent branching algorithm [34], which employs an angular-ordering scheme unlike the primarily hardness-ordered algorithm used in PYTHIA. This ensures a complete implementation of colour coherence of soft gluon emission in the parton showers following the hard collision, which was one of the major successes of the original HERWIG generator. Multiple partonic interactions in HERWIG are extended the soft non-perturbative region. The hadronisation is based on the Cluster model as described in Section (2.3.3). Similarly to PYTHIA, the parameters of the models used in HERWIG have to be tuned to experimental data [34].

HERWIG is based on THEPEG - the Toolkit for High Energy Physics Event Generation, which is a framework for the implementation of Monte Carlo event generators [55]. THEPEG only provides the generator infrastructure and does not depend on the physics models. The specific physics are implemented on top of it. In this analysis, two different versions of HERWIG were used to generate the event samples: HERWIG 7.1.3 and HERWIG 7.2.1. Both versions include spin correlations between particle production and decay in perturbative and non-perturbative interactions, but the newer version achieves full implementation of spin correlations in all stages of the event generation process by integrating the correlations into both the angular-ordered and dipole parton showers [56, 57]. The HERWIG 7 series is implemented in C++ and similarly to PYTHIA is the successor of the older HERWIG, which was a Fortran Monte Carlo package.

4.2.3 The POWHEG Method

The accuracy of Parton Shower (PS) simulation is evaluated on three different phase space variables per emission, with two of them (i.e. virtuality and angle) being associated with logarithmic divergencies in the squared matrix element and phase space product. The QCD processes in the Shower Monte Carlo (SMC) programs PYTHIA and HERWIG are calculated to leading order in the logarithmic level, but do not enforce NLO accuracy. The POWHEG (for Positive Weight Hardest Emission Generator) method provides a way of merging the existing SMC generators with NLO calculations (NLO+PS simulations) [58]. As previously mentioned, some approximate NLO corrections to the matrix elements are already included in the SMC programs, which essentially makes the merging of NLO calculations with parton shower simulations a problem of overcounting emissions. The

PowHEG method [58, 59] guarantees, that

- infrared-safe observables have NLO accuracy,

- collinear emissions are counted at leading-logarithmic level,

- the double logarithmic region (i.e. soft and collinear gluon emission) is treated correctly in the SMC program.

This last requirement is already fullfilled a priori in HERWIG, since its parton shower is inherently based upon an angular-ordered branching. The PowHEG method initiates the parton shower evolution at the hardness scale of the original input. Its shower formalism is based on the Sudakov form factor and produces emissions ordered in p_T-related hardness through a combined evolution of ISR and FSR. This is the same approach to parton shower simulation as is used in PYTHIA. The hardness definitions in the two programms differ however, which may lead to double- or under-counting of some phase space regions [60]. This is addressed in the PYTHIA machinery by shower vetoing: the parton shower may cover the full phase space using the PYTHIA hardness, even above the input scale, but any emission whose PowHEG definition of hardness is above the input threshold is vetoed. In general, the PowHEG framework allows matching to any SMC program that is either already p_T-ordered, or implements a p_T-based veto on the shower emissions. When interfaced to SMCs that use p_T-ordering, the double-logarithmic accuracy of the SMC is correctly retained. However, in the case of angular-ordered SMC programs, the double-log accuracy of the SMC is not sufficient to guarantee the double-log accuracy of the whole event.

5 Event Reconstruction

A requirement for the study of the spin observable $\cos\varphi$ is the adequate reconstruction of the $t\bar{t}$ system and its decay products including the spin analyzer. As discussed in Sec. 2.2.1, top quarks nearly always decay into a W boson and a bottom quark. This bottom quark as well as the two quarks from the hadronically decaying W initiate jets. The strange quark from this hadronic decay serves at the hadronic spin analyzer and is identified by pairing it with a charm flavoured jet. These heavy flavoured b and c jets can be identified through an experimental method called flavour tagging. Assigning the reco-level jets to the correct W boson and parent top quark is handled by the SPANet neural network.

5.1 Flavour Tagging

Heavy flavoured (HF) jets are any jets initiated through the decay of B hadrons for b jets or through the decay of D hadrons for c jets. These HF jets can be experimentally identified through a method called flavour tagging by exploiting some special characteristics of bottom and charm quarks. The decay of bottom quarks into either an up or charm quark through the weak interaction is suppressed by their respective CKM matrix elements V_{ub} or V_{cb}. As a consequence, B hadrons have lifetimes, that are sufficiently long ($\sim 10^{-12}$ s) [20] to reach the tracking detector before decaying at a secondary vertex some distance away from the primary vertex of the hard interaction as illustrated in Figure 5.1. The shortest distance from a particle's track to the primary vertex is called impact parameter. The existence of the secondary vertex gives the impact parameters of b jets a unique signature that can be used for their identification. Furthermore, bottom quarks are much more massive than anything they decay into. Their decay products therefore tend to have higher transverse momentum, leading to wider jets with higher invariant mass and higher multiplicities compared to light jets (u, d, s). Charm jets have similar characteristics. Charm quarks are much heavier than the down quark and their weak isospin partner, the strange quark, so their weak decay is not CKM suppressed. In return, they are lighter than bottom quarks, resulting in a shorter but comparable lifetime of D hadrons ($\sim 10^{-13}$ s) [20]. Consequently, c jets also produce a secondary vertex in the tracking detector. Since
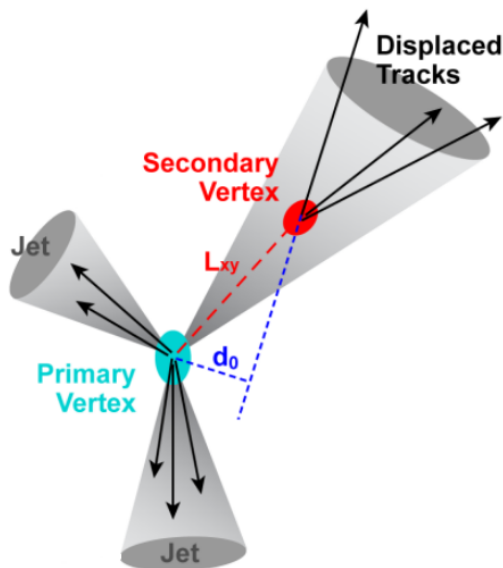
Abb. 5.1: Jets originating from heavy flavoured hadron decays are wider compared to light jets and have a large impact parameter d_0 as a result of the secondary vertex.

most kinematic variables for c jets typically lie somewhere inbetween light jets and b jets, the distinction between b and c jets is more challenging than differentiating between these heavy flavour jets and other light jets.

The flavour tagging for both the b as well as the c jets is carried out by the DL1r flavour tagger. This tagging algorithm is based on a fully connected multi-layer feed-forward neural network, that uses deep-learning classifiers to optimize the flavour tagging performance for Run II conditions at ATLAS [61, 62]. The DL1r algorithm has different operating points (OP), which are defined by the inclusive efficiency of correctly tagged b jets in the training sample. The 60% OP for example correctly tags 60% of all b jets. The DL1r tagger places events into five bins between the 60%, 70%, 77%, and 85% operating points bounded by the trivial 0% and 100% OPs according to their continuous tagging score. Operating points with greater sensitivity to b jets increase the inclusive efficiency but also decrease the purity at the same time. The 85% OP for example correctly tags almost every b jet but it does so at the expense of incorrectly tagging a higher percentage of other jets compared to lower OPs.

5.2 Event Reconstruction using SPANet

The final state partons from the resonance decay appear in the detector as observable jets. In order to extract the physics information from these events, it is therefore necessary to assign the correct particle origin to these jets as well as to determine from which of the
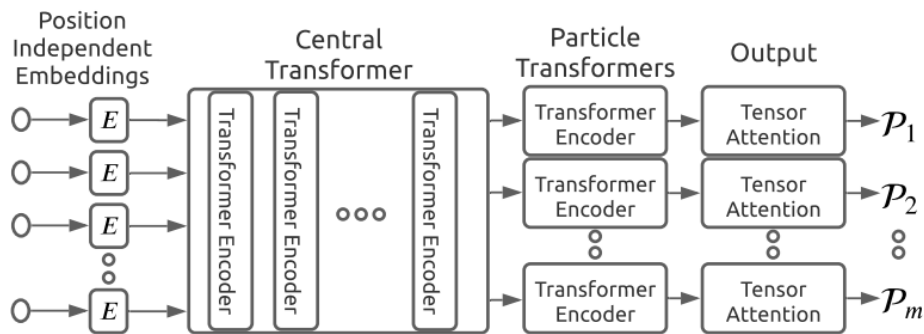
Abb. 5.2: A schematic of the high level architecture of SPANet.

parent top quarks they originated. The event reconstruction thus reduces to the problem of uniquely matching a set of particle labels to a collection of detector-level physics objects. The inherent difficulty of this task comes from the fact that the detector signature of jets especially from light quarks are virtually indistinguishable. The difficulty is even further enhanced because collisions typically produce more jets than expected from the parton-level final state.

In this analysis, the jet-parton assignment is accomplished through the use of SPANet, a symmetry preserving attention neural network for generalized permutationless set assignment [63, 64]. SPANet implements the χ^2 minimization technique, which assigns a score to every possible permutation of jets. For a semileptonic $t\bar{t}$ decay with at least four jets, two of which are jets, and at least one lepton, the χ^2 would be defined as

$$\chi^2 = \frac{(m_{b_1qq} - m_{b_2l\nu})^2}{\sigma_t^2} + \frac{(m_{qq} - m_W)^2}{\sigma_W^2} + \frac{(m_{l\nu} - m_W)^2}{\sigma_W^2}, \tag{5.1}$$

where m always represents the invariant mass of the jets and particles denoted by its subscripts with $m_W = 80.399\,\text{GeV}$ [20] being the measured W boson mass, and σ_t and σ_W are the widths of the resonances in the dataset fitted to a Gaussian. The χ^2 is evaluated for every possible permutation of jets and the parton assignment with the lowest score is ultimately chosen. In cases with only one lepton to choose from, the contribution from the leptonic W decay can be neglected. There are a few ways to reduce the number of permutations that have to be tested. The b jets are identified through flavour tagging, so that only these jets are allowed in the place of b quarks. This succesfully reduces the permutations but also makes it impossible to find the correct assignment if the b jet was mistagged. There are also symmetries of the event, that can be exploited to greatly reduce the number of permutations. For example, since the electric charge of the initiating particle cannot be reliably measured from a jet, a quark and its antiquark leave

the identical signatures in the detector and hence no meaningful distinction between the two can be made. Additionaly, the reconstruction may be insensitive towards exchanging particle labels. For example, for most physics objects the reconstruction of a W boson is invariant under the switching of labels assigned to the quark and antiquark.

The general architecture of SPANet is visualized in Fig. 5.2. It consists of four unique components: jet-independent embeddings convert the jet represented by its four-momentum into a latent space representation; a central stack of transformer encoders that contain multi-head self-attention layers and learn contextual relationships; additional branches of transformer encoders for each particle in the resonance decay; and lastly tensor-attention output layers that produce the final jet-parton assignment.

5.3 Reconstruction of the Top Quark

The final state objects produced in the semileptonic resonance decay of the $t\bar{t}$ system include an electron or muon + neutrino from the leptonically decaying W boson as well as two jets from the hadronically decaying W. Both top quarks also contribute one b jet. These simple physics objects serve as the basis for the reconstruction of more complex objects like the W and top quark.

5.3.1 Particle-Level Objects

The definitions of these objects on particle-level are chosen to closely match the experimentally reconstructed objects. They are defined via the following conventions for studies at ATLAS [65]:

- **Electrons** and **Muons** are defined in their bare state as the final state electrons or muons in the generator record after QED FSR. These bare leptons are then dressed with a cone of photons using an anti-k_T clustering with a small distance parameter of $R = 0.1$, since the FSR photons are mostly collinear leptons. Furthermore, they are required to be *prompt particles*, which means that they were produced in the main collision of the event and not in the decay of physical hadrons or its decendants.

- **Neutrinos** do not leave a signature in the detector but they can be inferred from the transverse momentum missing in the event reconstruction. On particle-level, the neutrino is nonetheless treated as a detectable particle in the same way as a charged lepton and is also required to not come from hadron. The particle-level definition of missing transverse momentum E_T^{miss} is then the sum of all neutrinos, giving the

true transverse vector sum of particles from the hard process, that are invisible to a detector.

- **Jets** are defined using the anti-k_T clustering algorithm with a distance parameter of $R = 0.4$ for ATLAS. The algorithm loops over all stable particles in the generator record, i.e. particles with a mean lifetime $> 0.3 \times 10^{-10}$ s, excluding the prompt electrons, muons, neutrinos, and the photons that they were dressed with.

- **HF jets** are any jets that contain a weakly decaying heavy flavoured hadron with initial $p_T > 5$ GeV. A jet is considered a b jet if it contains at least one b hadron and a c jet if it contains at least one charm hadron but no b hadrons. Since these HF hadrons have too short of a lifetime to be counted as stable particles, they are not initially included in the clustering of particle-level jets. To account for this, the heavy flavoured hadrons are added to the clustering input with infinitely small four-momentum, only retaining information about their track. This does not affect the reconstruction but makes it possible to identify which tracks are clustered into which jets. This process is called *ghost association.*

5.3.2 Hadronic and Leptonic Pseudo-Top

The particle-level top quark, called pseudo-top, can be defined with the help of the final state objects as defined above. A pre-selection is applied to identify a semileptonic $t\bar{t}$ decay. A signal event is required to have exactly one electron or muon, and no other charged leptons. It is also required to have ≥ 4 jets of which at least two are b jets. The two b jets with the highest p_T are then selected for the pseudo-top definition. Pseudo-tops are furthermore categorized as either hadronic or leptonic depending on the decay mode of the W boson [65, 66].

The leptonic pseudo-top is constructed from the charged lepton, neutrino, and assigned b jet. A complete construction therefore requires the neutrino's longitudinal momentum $p_{z,\nu}$, which can be obtained from four-momentum conservation in the decay of the physical W boson using its measured invariant mass m_W and the missing transverse momentum associated with the neutrino, $p_{x,\nu}$ and $p_{y,\nu}$,

$$(E_l + E_\nu)^2 - (p_{x,l} + p_{x,\nu})^2 - (p_{y,l} + p_{y,\nu})^2 - (p_{l,\nu} + p_{z,\nu})^2 = m_W^2. \tag{5.2}$$

This relation produces a quadratic equation that can be solved for $p_{z,\nu}$ [66]. In case of a two-fold ambiguity, the solution with the smaller magnitude is chosen. From the two possible b jet candidates the jet with the smaller angular distance ΔR to the charged

lepton is selected. The leptonic pseudo-top can then be formed by combining the four-momenta of the assigned b jet and the leptonic W.

The hadronic pseudo-top is constructed from the hadronically decaying W boson and the remaining b jet. The hadronic W is formed by looping over all light jets and choosing the combination, which is closest to the invariant W mass.

6 Systematic Uncertainties from Parton Shower Modelling

The differences in the kinematic properties of the $t\bar{t}$ system between the Powheg+Herwig and Powheg+Pythia samples give rise to systematic uncertainties on the shape of the $\cos\varphi$ distribution. To estimate and comprehend these parton shower modelling uncertainties the event topology of both generators is compared with special attention on the SPANet reconstruction. Also, the two versions Herwig 7.1.3 and Herwig 7.2.1 are compared to estimate the impact of new developments in the Herwig generator on this particular analysis [57]. The newer Herwig 7.2.1 sample was produced through a full simulation, while the older Herwig 7.1.3 sample was produced with the fast simulation scheme. The Pythia 8.2 samples they are compared to at any point in this analysis were produced using the same method, respectively.

6.1 Spin Observable and Kinematic Variables

First, the entanglement measure D is calculated and a selection of kinematic variables, that impact the top reconstruction and consequently $\cos\varphi$, is compared for both generators.

Event Selection

To identify the $t\bar{t}$ events that decay through the semileptonic channel, a pre-selection is applied. On reco-level each event is required to have

- exactly one e or μ with $p_T > 28\,\text{GeV}$

- a total of four or more jets each with $p_T > 25\,\text{GeV}$

- two or more b-tagged jets

- missing transverse momentum > 20 GeV

Tab. 6.1: D values on parton-, particle-, and reco-level for POWHEG+PYTHIA and the different POWHEG+HERWIG samples with relative differences. The Py8.2 sample on the left was produced via fast simulation and the one on the right via full simulation.

	Py8.2	He7.1.3	Δ/Py	Py8.2	He7.2.1	Δ/Py	$\Delta_{He}/\mathrm{He7.1.3}$
D_{parton}	-0.436	-0.442	$1.4\,\%$	-0.435	-0.441	$1.6\,\%$	$0.2\,\%$
$D_{particle}$	-0.483	-0.535	$10.8\,\%$	-0.482	-0.449	$6.9\,\%$	$16.1\,\%$
D_{reco}	-0.266	-0.249	$6.4\,\%$	-0.269	-0.250	$7.1\,\%$	$0.4\,\%$

The p_T cuts on the charged leptons are imposed to ensure that the events pass the ATLAS lepton trigger. As discussed in Sec. 2.2.3, the $t\bar{t}$ system is produced in the desired spin singlet state if its invariant mass is close to production threshold. Also, the down-type spin analyzer from the hadronic W is identified through charm-tagging, as it is impossible to experimentally distinguish between first generation quarks, hence the focus on the second generation. This yields two more conditions for the final event selection:

- the invariant $t\bar{t}$ mass has to fulfill: $m_{t\bar{t}} < 390\,\mathrm{GeV}$

- the hadronic W decay has to contain a c jet

SPANet uses its own internal flavour-tagging for the jet-parton assignment. The event selection in this analysis however relies on the b- and c-tagging of the DL1r tagger. An event counts as having a c jet if none of the jets, that were assigned to the hadronic W by SPANet, are tagged by the 60% DL1r operating point and if their continuous tagging scores do not fall into the same bin. The jet assigned to the higher purity bin is then chosen to be the up-type jet and the jet assigned to the lower purity bin is chosen as the spin analyzer.

The p_T cuts are applied to account for detector acceptance. On particle-level this does not need to be taken into consideration and the pre-selection described in Sec. 5.3 is applied to particle-level objects instead. The flavour-tagging is done by ghost-association and the top quarks are reconstructed according to the pseudo-top construction procedure. On parton-level this is even more straigtforward, as the signal events containing a charm on the hadronic side and an electron or muon on the leptonic side can be directly selected using the particle identifiers from the generator record.

Calculation of D from the $\cos\varphi$ distribution

The $\cos\varphi$ distributions are obtained by boosting the spin analyzers to the system of their respective reconstructed parent top quark and calculating the dot product between their
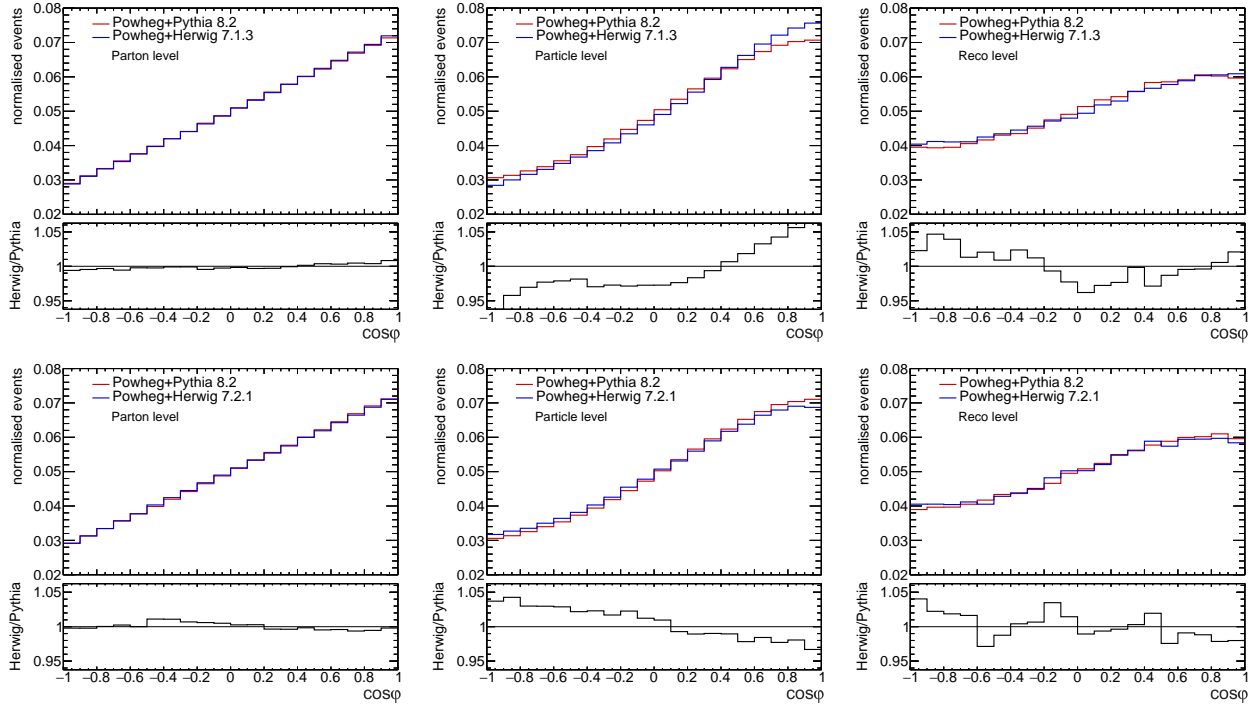
Abb. 6.1: Normalised $\cos\varphi$ distributions on parton-, particle-, and reco-level for Powheg+Herwig 7.1.3/Powheg+Herwig 7.2.1 and Powheg+Pythia 8.2.

momentum directions. Figure 6.1 shows the distributions for the different samples. The parton-level samples display the expected linear relationship between the normalised differential cross-section and the cosine of the opening angle between the two spin analyzers in Eq. 2.7 with very minimal difference between SMC generators. The particle-level distributions however showcase large deviations between the different SMC programs. This causes large systematic uncertainties on the entanglement sensitive D value. Table 6.1 lists the different values for D obtained through Eq. 2.8 on each level for the different generators. The statistical uncertainty in D can be neglected in case of large event numbers as it decreases with $1/\sqrt{N}$, where N is the number of selected events [67]. On parton-level, the D values for all samples fullfill the requirement of $D < -1/3$ from Eq. 2.9. Top quarks produced at treshold at the Lhc are therefore expected to be entangled. The two Pythia samples show only very little discrepancy as is expected from the different simulation schemes.

On particle-level, the distributions still showcase their linear character but are more s-shaped due to the blurring of parton-level theory as a consequence of the phenomenological models in the event generation as well as event reconstruction. Here, the slope of the Herwig 7.1.3 sample is substantially steeper compared to Pythia 8.2, leading to a considerable difference in the resulting D values of 10.8%. The newer Herwig 7.2.1
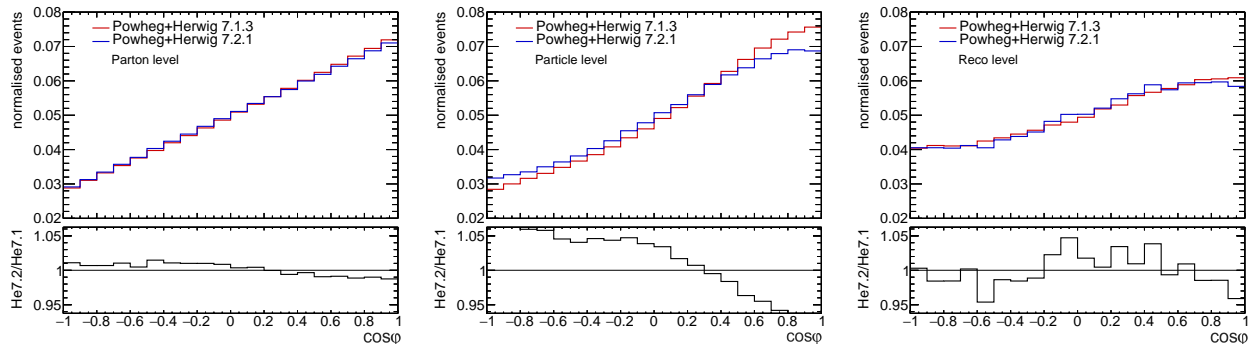
Abb. 6.2: Normalised $\cos\varphi$ distributions on parton-, particle-, and reco-level for POWHEG+HERWIG 7.1.3 and POWHEG+HERWIG 7.2.1.

sample on the other hand displays the exact opposite trend, as the distribution is overall flatter relative to PYTHIA, reducing the differences in the slope to 6.9%. It also matches the distribution better overall. At the lower and especially the upper limit of the $\cos\varphi$ domain, the particle-level HERWIG samples show larger disagreements with PYTHIA but also with each other. This trend between the two HERWIG samples is already visible in the parton-level distributions and only grows more significant after parton showering as can be seen in Figure 6.2. As already mentioned, the newer HERWIG version uses an improved spin correlation algorithm that incorporates the correlations into all stages of event generation, including particle production and both perturbative and non-perturbative decays as well as both the angular-ordered and dipole parton showers. As a consequence, the two HERWIG samples show considerable disagreement on particle-level with a difference of 16.1 % in the D values.

On reco-level, the D value falls outside the $-1/3$ threshold as detector and reconstruction effects lead to a considerably shallower distribution. These reco-level values reflect the expected distribution obtained from real data samples. These results would then have to be mapped to the corresponding parton-level distribution to compare it to theory. A measured value of $D \approx -0.26$ would therefore demonstrate entanglement in the $t\bar{t}$ system as the corresponding parton-level value satisfies the Peres-Horodecki-criterion according to these Monte Carlo samples. The differences in the slope between the two generators amount to 6.4 % for the older and a larger 7.1 % for the newer HERWIG version even though the distribution of the newer version matches PYTHIA better overall. Compared to particle-level, the two HERWIG samples show a smaller deviation. This suggests that the differences in the particle-level distribution in HERWIG are evened out as a consequence of the detector simulation and event reconstruction.

Kinematic Variables
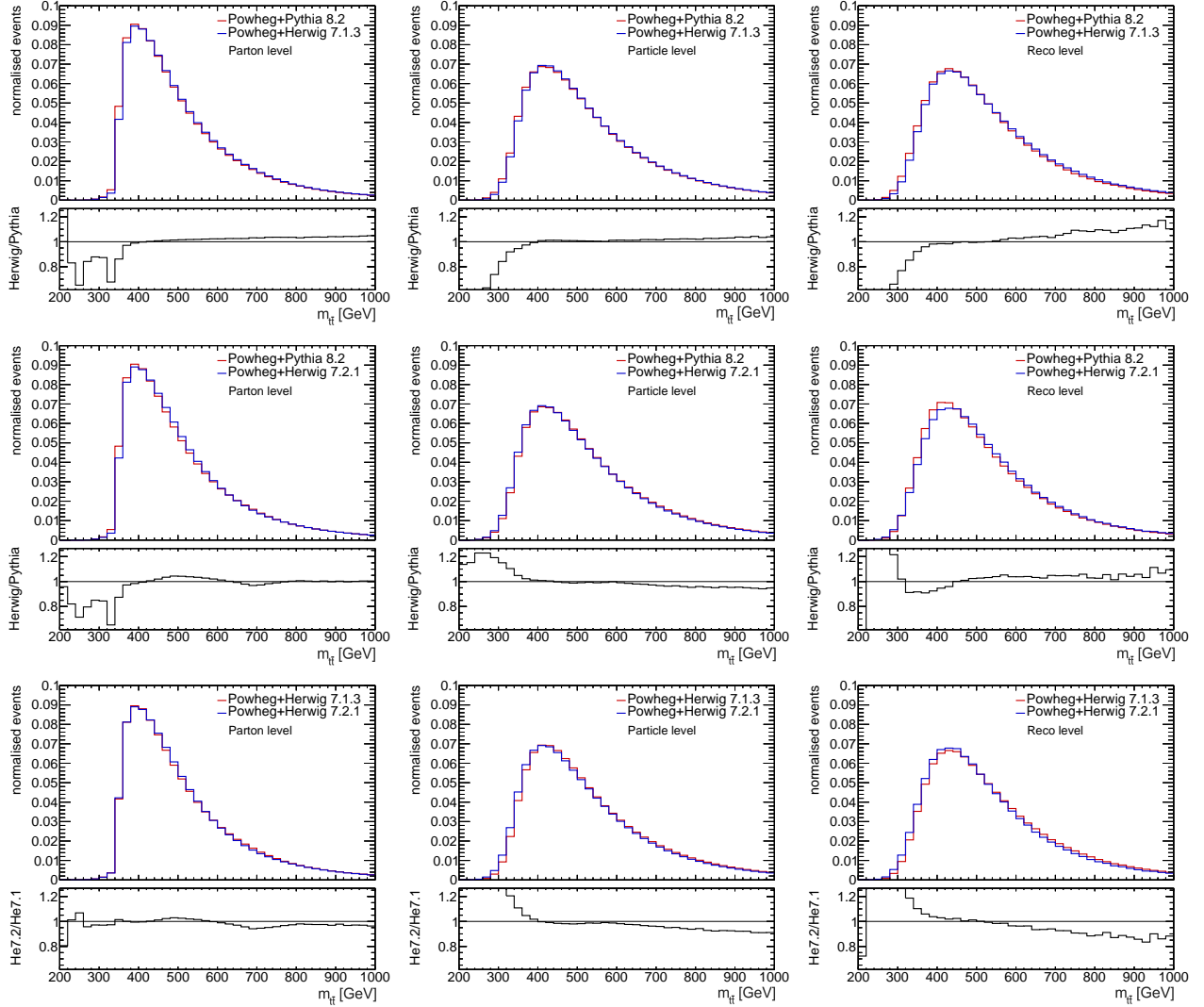
Abb. 6.3: Normalised $m_{t\bar{t}}$ distributions on parton-, particle-, and reco-level for POWHEG+HERWIG 7.1.3/POWHEG+HERWIG 7.2.1 and POWHEG+PYTHIA 8.2.

The $\cos\varphi$ reconstruction is dependend on a number of kinematic variables. The invariant mass $m_{t\bar{t}}$ of the $t\bar{t}$ system for example is used in the event selection to reject events in which the top pair is not produced in a spin singlet state. Figure 6.3 shows the $m_{t\bar{t}}$ distribution for the semileptonic resonance decay obtained for each sample. The characteristic Breit-Wigner shape is shifted to the right of the measured $t\bar{t}$ mass of $m_{t\bar{t}} = 345\,\text{GeV}$ [20] with a steep decline on the lower mass side due inherent cuts on low-p_T jets/partons in the samples. On parton-level, the different samples match very closely in mass regions with sufficient statistics. The blurring of energy and momenta of the partons through hadronisation and jet reconstruction leads to wider distributions on particle-level, which

are very closely replicated by the reco-level distributions. On particle-level Herwig 7.1.3
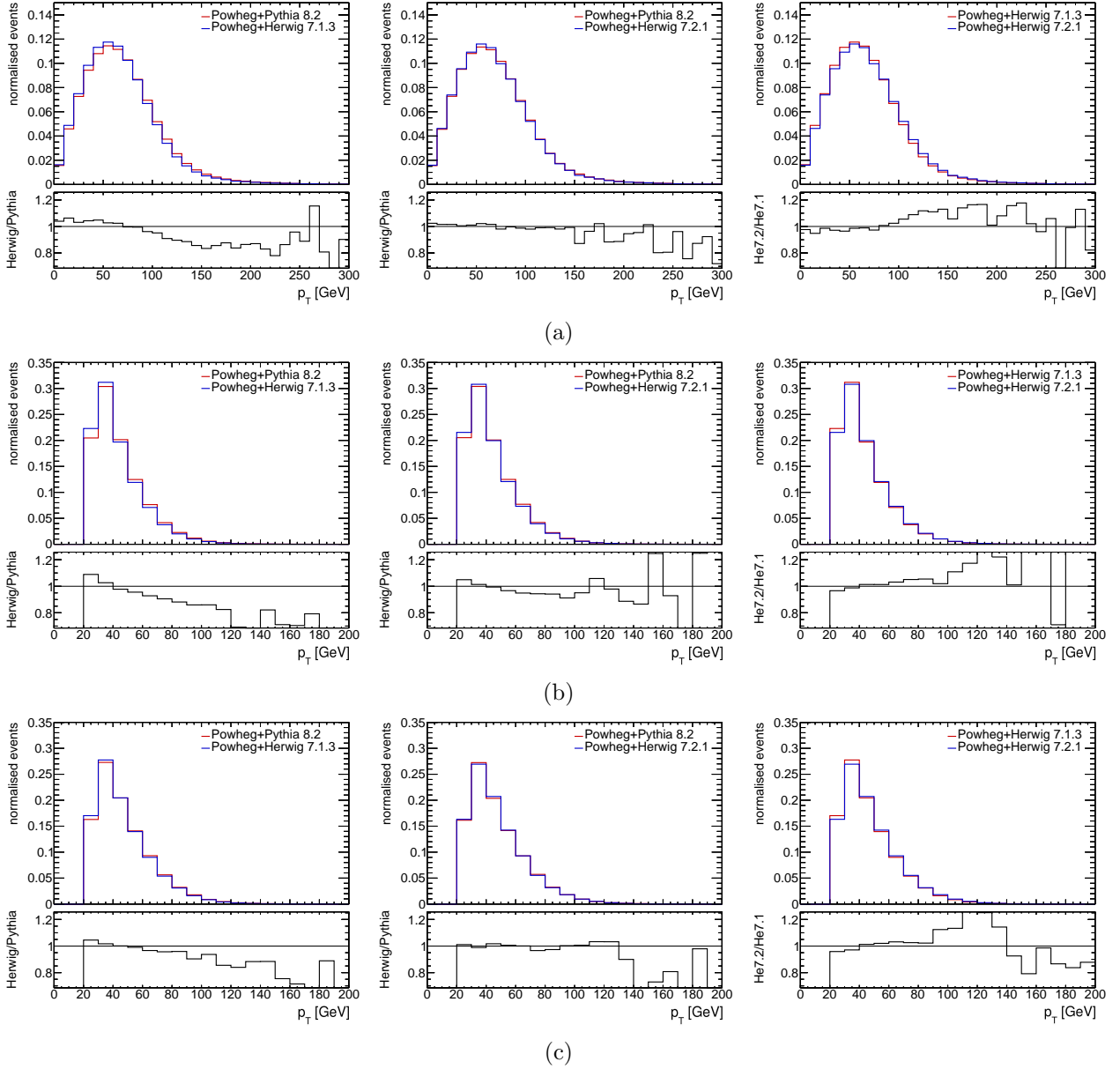
Abb. 6.4: Normalised p_T distributions of (a) the *hadronic top* on reco level, of (b) the *down type jet*, and of (c) the *up type jet* for Powheg+Herwig 7.1.3, Powheg+Herwig 7.2.1, and Powheg+Py 8.2.

produces more events below the mass cut relative to Pythia while Herwig 7.2.1 produces less events in that region. Figure 6.4a suggests that this distribution is inherited from the mass of the reconstructed hadronic top. The transverse momenta of the down- and up-jet, that make up the hadronic top, are portrayed in Fig. 6.4b and 6.4c. Because of the V-A structure of the CP-violating W boson decay, the up jets receive a higher share of the transverse momentum from the parent W compared to the down jets, which can be
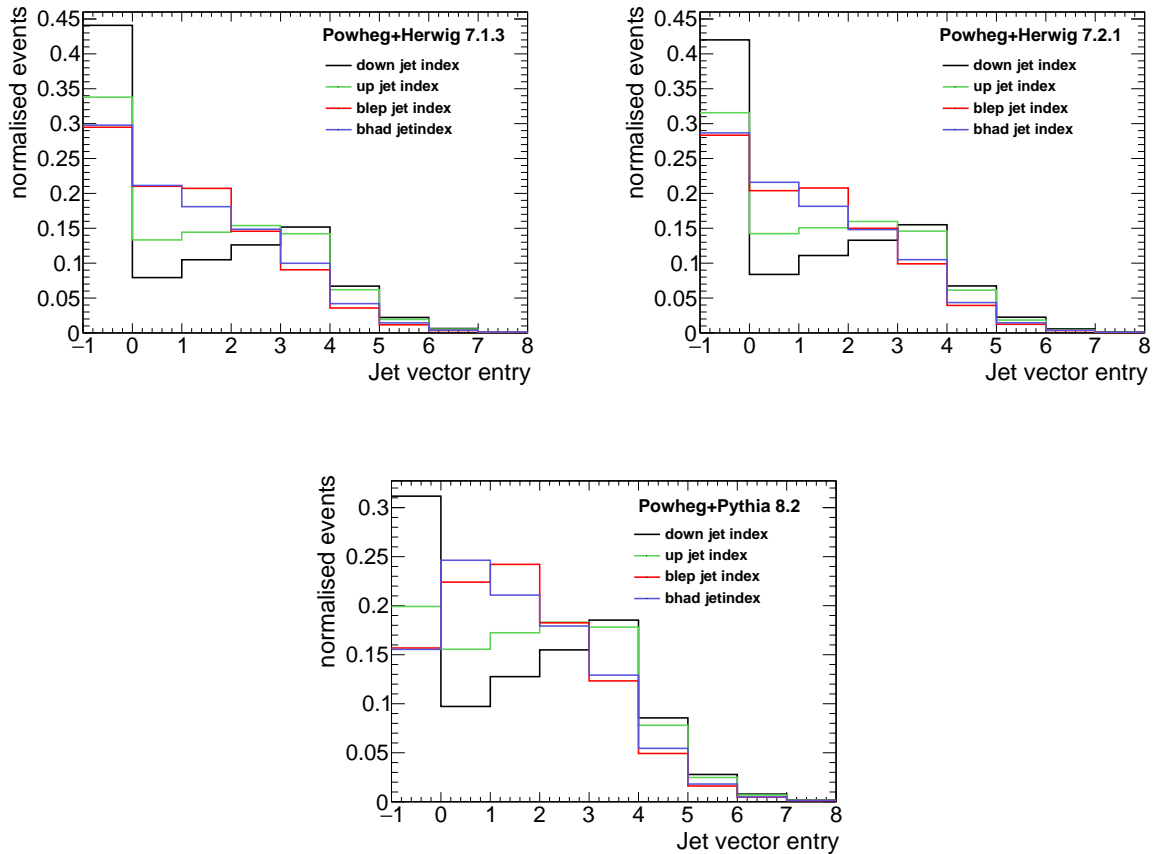
Abb. 6.5: Normalised distribution of particle-level jet vector entries for POWHEG+HERWIG 7.1.3, POWHEG+HERWIG 7.2.1, and POWHEG+PYTHIA 8.2 (fastsim). Jets in the far left bin are counted as missing as they cannot be matched to a parton. Jets are arranged from left to right according to their transverse momentum in a given event, s.t. the jet with the highest p_T gets placed in the second most left bin, and the jet with the second highest p_T gets placed to his right etc.

seen in the graphs. Between the different generators PYTHIA has a higher percentage of higher-p_T down jets than HERWIG.

Figure 6.5 shows how the four relevant jets are sorted according to their transverse momentum with higher p_T jets arranged to the left. The very left column indicates events in which that particular jet is missing on particle-level. A jet technically counts as missing on particle-level if it cannot be matched to a parton. A parton and jet are matched if their distance in angular space fullfills $\Delta R < 0.3$. Only events that passed the reco level selection are included in Fig. 6.5. The high number of missing down jets is problematic in the sense that SPANet will assign the down jet label to any other jet in that case. Since these jets usually do not carry the same spin information, this may lead to uncertainties in

Abb. 6.6: Normalised distribution of the total number of jets in a given event for Powheg+Herwig 7.1.3, Powheg+Herwig 7.2.1, and Powheg+Pythia 8.2 (fastsim).

the resulting $\cos\varphi$ distribution. As expected, the down jet typically has lower transverse momentum compared to the up type jet, which is the case for all generators. In general, the Pythia samples have far fewer missing jets than both Herwig samples. Figure 6.6 shows how many jets are generated in a semileptonic $t\bar{t}$ event by the different SMC programs on average. The event selection requires at least four jets but most events produce more than the minimum threshold with some events going high as ten, mostly because of gluon jets. It is immediately obvious that Pythia 8.2 produces a higher fraction of events with exactly four jets than Herwig 7.1.3, while the number of jets in Herwig 7.2.1 events closely matches its Pythia counterpart. These kinematics impact the event reconstruction and will therefore be examined in the context of SPANet.

6.2 Differences in the SPANet Event Reconstruction

The SPANet neural network is used to reconstruct the hadronic top and assign the b jet belonging to the leptonic top. To understand how the SPANet reconstruction is impacted by the specific SMC program, the reconstruction results are examined based on the event topology for both generators.

6.2.1 SPANet Performance and Jet Topology

SPANet assigns two scores to each event expressing its confidence in succesfully reconstructing the hadronic and leptonic top with correctly reconstructed event averaging a higher score. The scores for both are compared in Fig.6.7. Both Herwig and Pythia have mostly overlapping distributions while the older herwig has a more spread out distribution. The ratio plots clearly show trends between Pythia 8.2 and Herwig 7.1.3, as
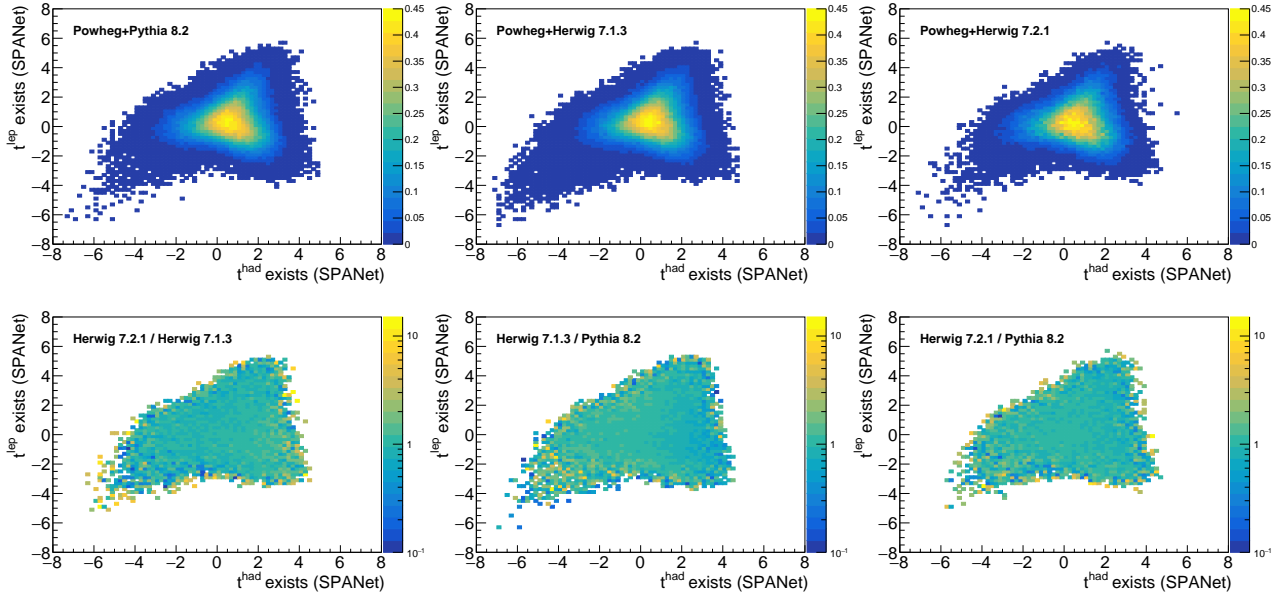
Abb. 6.7: Top: Normalised distributions of events depending on the SPANet hadronic top score and leptonic top score for POWHEG+HERWIG 7.1.3, POWHEG+HERWIG 7.2.1, and POWHEG+PYTHIA 8.2 (fastsim). The z axes represent percentages. Bottom: Ratio plots of the different distributions. The HERWIG 7.2.1 sample is still divided by the fullsim PYTHIA sample.

the latter is more likely to have a lower hadronic top score and a higher margin of events with both scores in the negative range. This stays the same when comparing HERWIG 7.1.3 to 7.2.1, which leads to PYTHIA and HERWIG 7.2.1 having relatively good agreement. To assess the SPANet reconstruction, define the following categories for reco-level events:

- **Correctly Matched (cm):**
  - *hadronic top:* b jet is correctly matched, up and down jets are correctly matched or swapped
  - *leptonic top:* b jet is correctly matched

- **Non-reconstructable (nrec):**
  - *had. top & lep. top*: At least one jet is missing

- **Incorrectly Matched (incm):**
  - *had. top & lep. top*: All jets exist but not correctly matched as defined above

The DL1r c-tagging accounts for events with swapped up and down jets. With these definitions, the SPANet reconstruction performance can be evaluated for the different generators. Figure 6.8 shows the results of the hadronic top reconstruction. As discussed
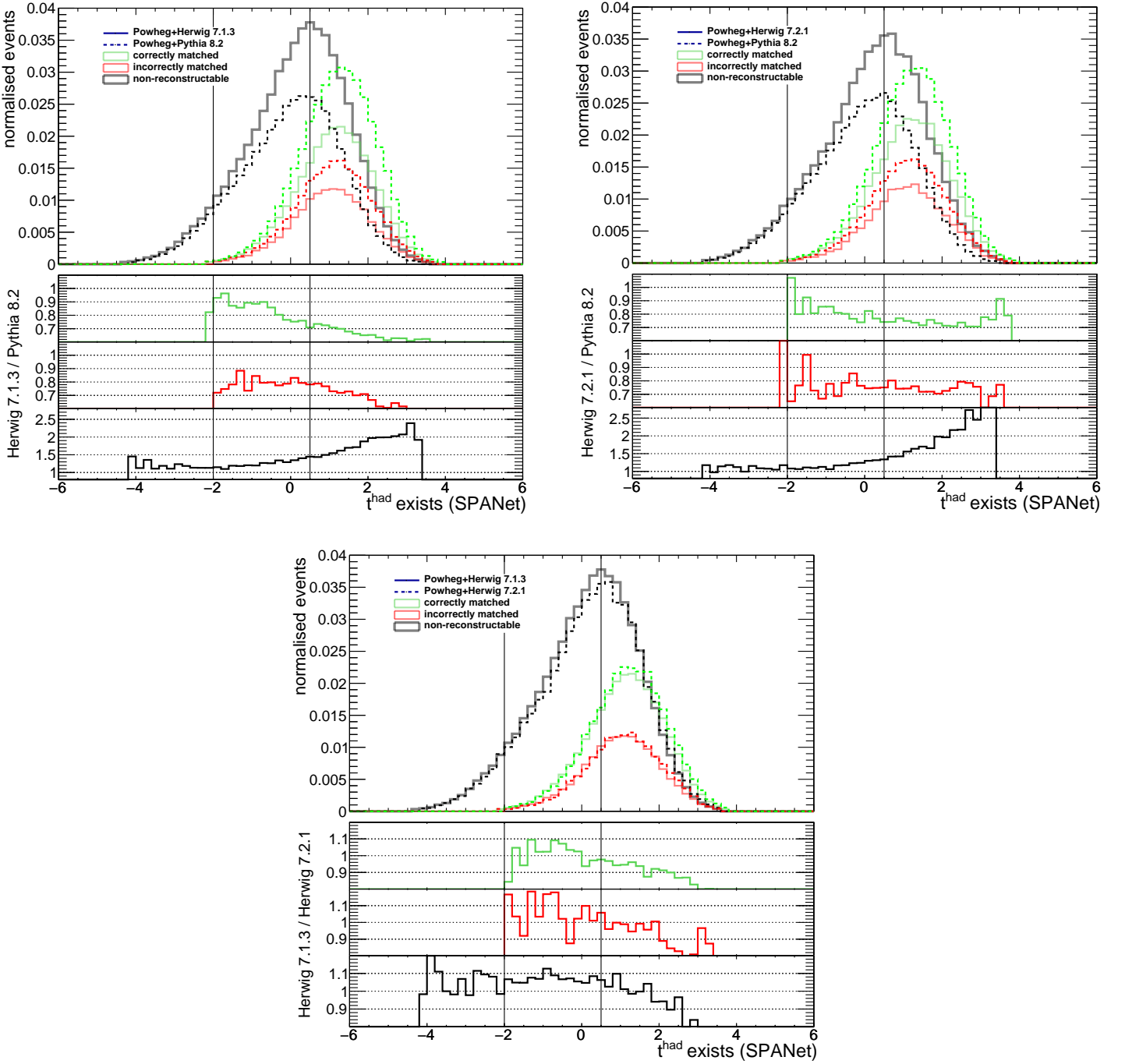
Abb. 6.8: Normalised distribution of the (in-)correctly matched and non-reconstructable events depending on the hadronic top reconstruction score from SPANet for Powheg+Herwig 7.1.3/ Powheg+Herwig 7.2.1 compared to Powheg+Pythia 8.2. The vertical lines at -2 and 0.5 define three t^{had} existence regions.

(a)

(b)
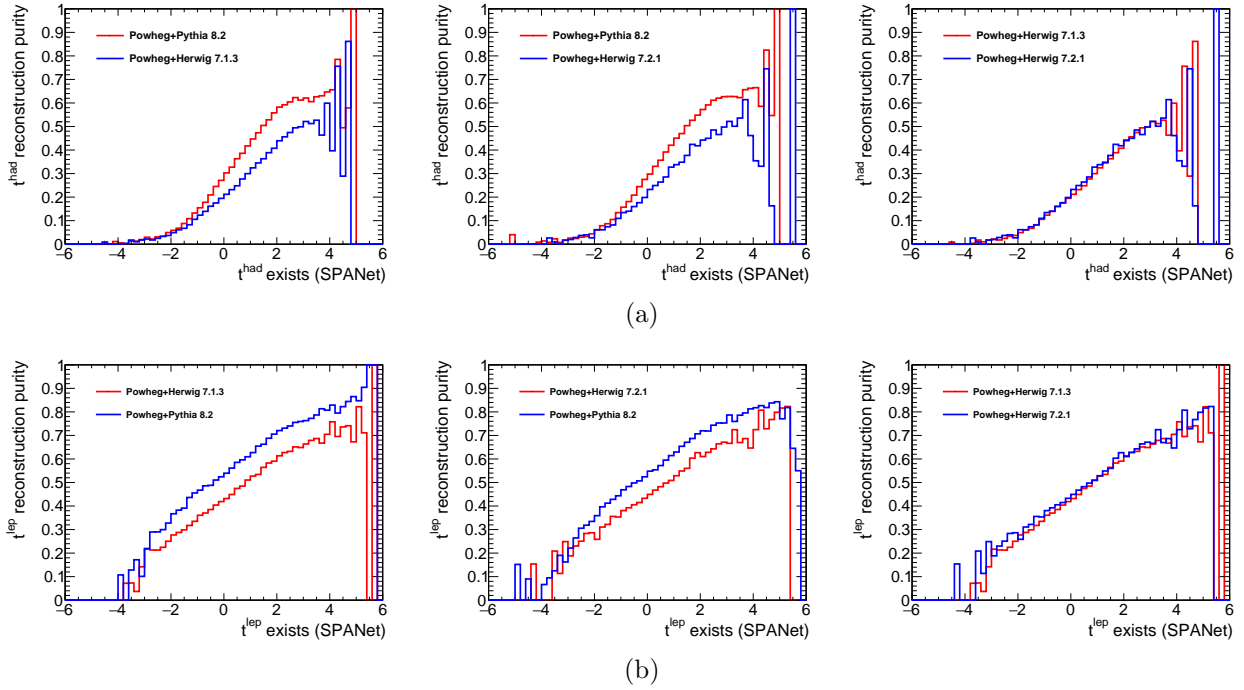
Abb. 6.9: Purity of (a) the reconstructed hadronic top and (b) the reconstructed leptonic top depending on the t^{had} existence score for Powheg+Herwig 7.1.3, Powheg+Herwig 7.2.1, and Powheg+Pythia 8.2.

before, Pythia has less non-rec. events on particle level, which translates to reco-level. As a result, the Pythia distributions have a higher percentage of fully reconstructed events. Notably though, the incorrectly matched distribution grows about the same rate when comparing it to the Herwig samples. The two Herwig samples do not showcase any major differences beside the small advantage of Herwig 7.2.1 as a consequence of the slighty better jet-parton matching. The peak of the *cm* graph corresponds to a minimaly higher t^{had} existence score than the *incm* peak, while they are both shifted to the right of the non-reconstructable graph. This invites the introduction of three t^{had}-score regions with limiters -2 and 0.5, s.t. the *low* region only contains non-reconstructable events, the *middle* region contains some *cm* and *incm* events but mostly still *nrec*, and the *high* score region has the highest purity of correctly matched events. The purity P defined by,

$$P = \frac{N_{cm}}{N_{cm} + N_{incm} + N_{nrec}},$$

is plotted in Fig.6.9a for the hadronic top and in Fig.6.9b for the leptonic top. To analyze the difference between events in each region, the non-reconstructable events are unraveled in Fig.6.10. This figure shows the rate at which a certain jet is missing among the
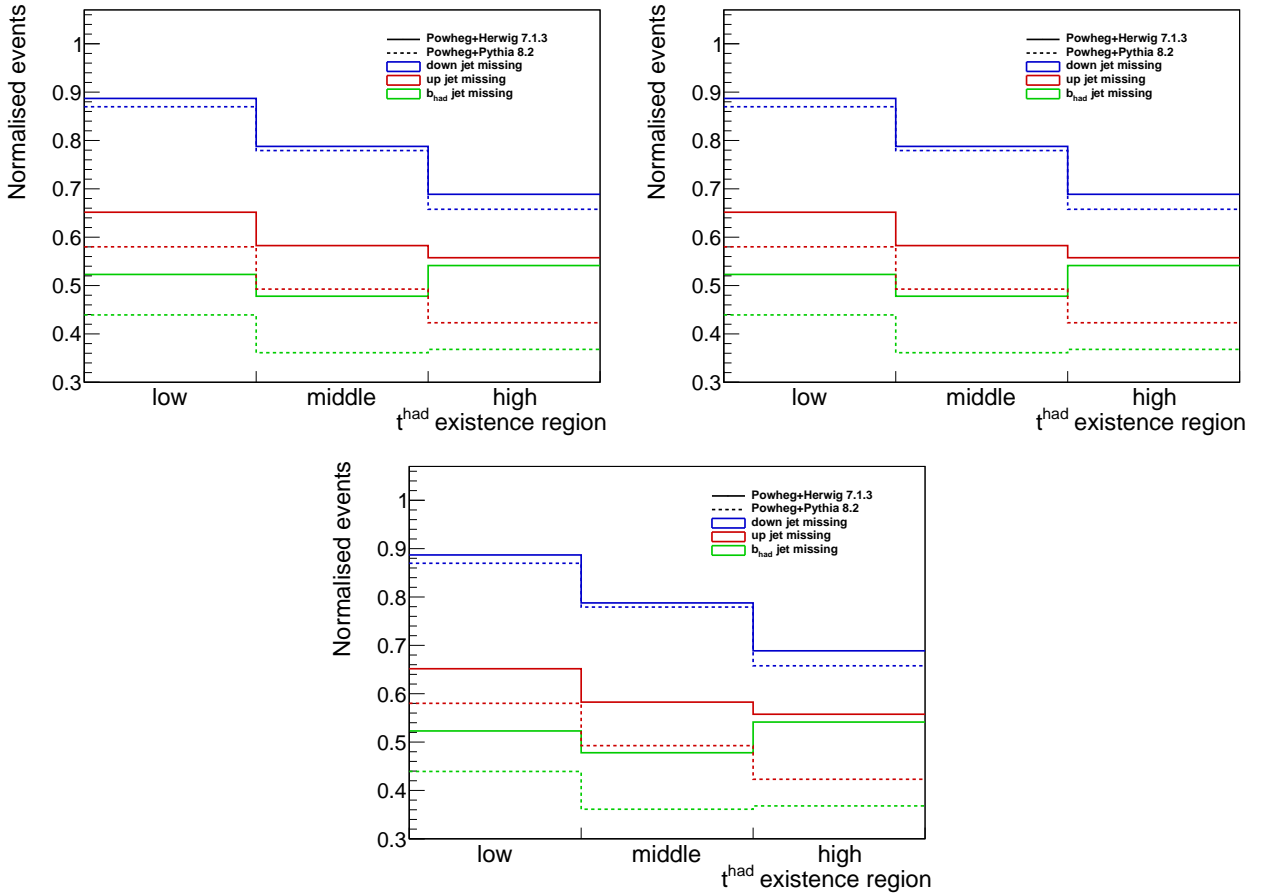
Abb. 6.10: Rate of missing jets for the low, middle, and high hadronic top score regions for Powheg+Herwig 7.1.3, Powheg+Herwig 7.2.1, and Powheg+Pythia 8.2.

non-reconstructable events in that region. As expected, most of these events do not have a down jet on particle level. The distributions show little difference between the samples. The ratios at which a b or up jet is missing on the other hand shows a larger difference between Pythia and Herwig. In particular in the case of a Herwig generated sample, the missing rate of the hadronic b jet even rises when moving from the *middle* to the *high* region while the missing rate of the up type jet also stays fairly level. Only the down jet shows a clear downward trend between all samples when moving to a higher hadronic top existence score. Therefore, the down jet most likely has the largest impact on the event reconstruction by spanet and events with a topology that favours a reliable down jet reconstruction have a better chance of being succesfully reconstructed as a whole. To investigate this even further, one can look at the exclusive jet makeup of non reconstructable events. Figure 6.11a and 6.11b depict these exclusive missing jet distributions for the hadronic top reconstruction. The same coloured bars are respectively normalized to

(a)

(b)
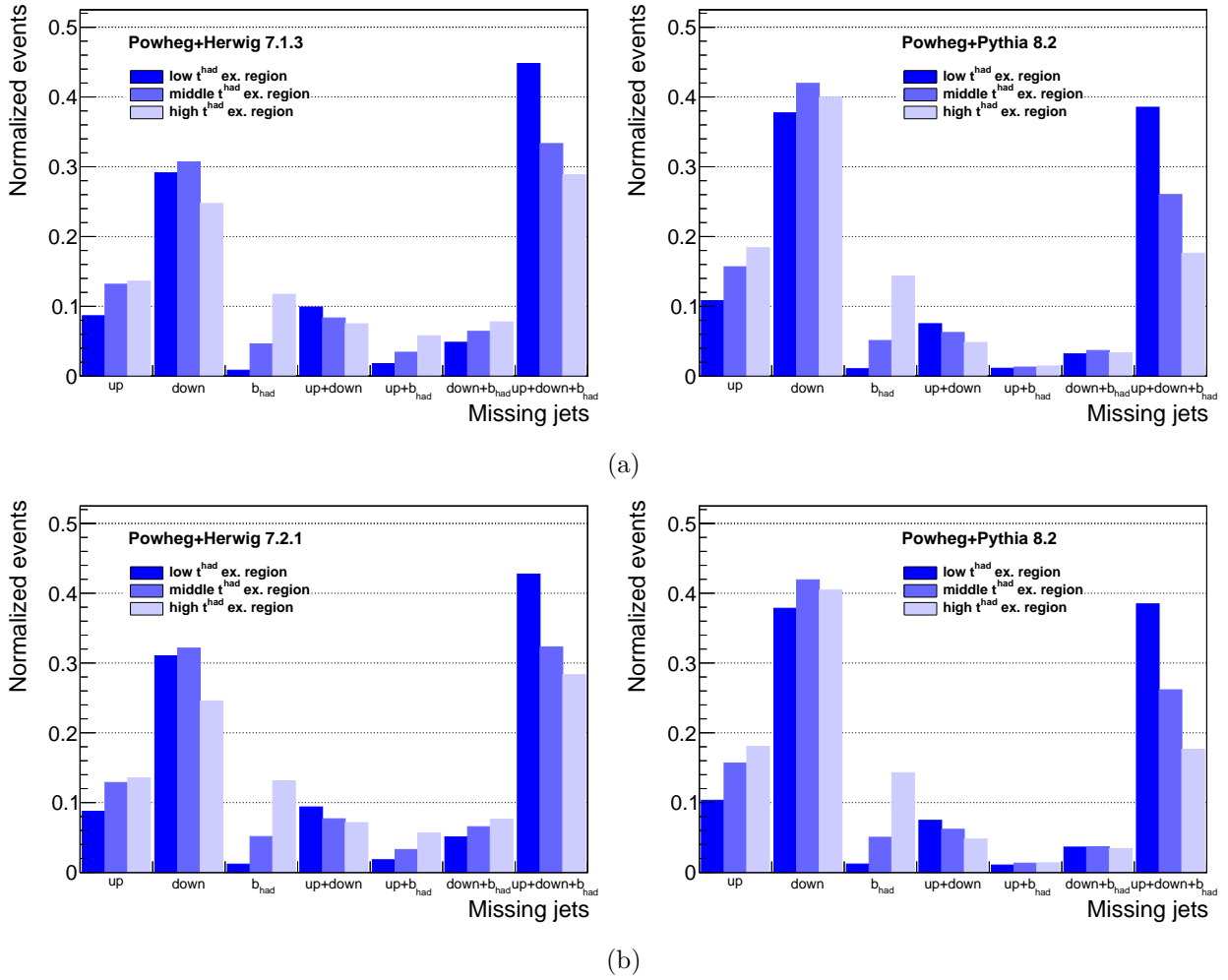
Abb. 6.11: Normalised distribution of missing jet combinations for the low, middle, and high hadronic top existence regions for (a) Powheg+Herwig 7.1.3 and Powheg+Pythia 8.2 (fastsim) and (b) Powheg+Herwig 7.2.1 and Powheg+Pythia 8.2 (fullsim).

1. Events with only a down jet missing are very frequent in all regions especially with the Pythia samples. In general, Pythia shows a high percentage of single missing jets. On the contrary, non-reconstructable Herwig events are missing more than one jet more often, especially any combination that contains a b jet as can be inferred from Fig.6.10 already. In general, combinations with a missing down jet are more frequent in the low existence score region compared to the higher region. In Figure 6.12 the three reconstruction categories are plotted in depence of the leptonic top existence variable assigned by SPANet. In contrast to the hadronic top reconstruction, the *nrec* and *incm* distributions are essentially completely contained within the *cm* distributions, so there are no possible cuts on the leptonic top variable, that cut out more *nrec* than correctly matched events.
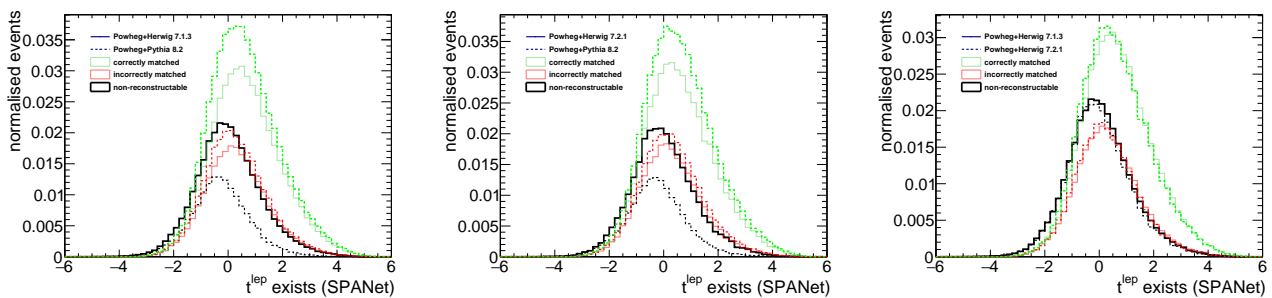
Abb. 6.12: Normalised distribution of the (in-)correctly matched and non-reconstructable events depending on the leptonic top reconstruction score from SPANet for Powheg+Herwig 7.1.3, Powheg+Herwig 7.2.1, and Powheg+Pythia 8.2.

Tab. 6.2: D values reco-level for Powheg+Pythia and the different Powheg+Herwig samples with relative differences. The left Py8.2 sample was produced via fast simulation and the one on the right via full simulation. A cut on the hadronic top existence SPANet variable was applied to the reco-level event.

	Py8.2	He7.1.3	Δ/Py	Py8.2	He7.2.1	Δ/Py	Δ_{He}/He7.1.3
D_{reco}	-0.266	-0.249	$6.4\,\%$	-0.269	-0.250	$7.1\,\%$	$0.4\,\%$
$D_{reco,SPANet}$	-0.368	-0.353	$4.1\,\%$	-0.371	-0.352	$5.1\,\%$	$0.3\,\%$

Tab. 6.3: Weighted number of events, that passed the event selection with and without the SPANet cut.

	He7.1.3	Py8.2 (fast)	He7.2.1	Py8.2 (full)
N_{select}	29590	34034	33117	33455
$N_{select,SPANet}$	16309	20150	18984	19777
Statistics cut	$45\,\%$	$41\,\%$	$43\,\%$	$41\,\%$

Similar to the hadronic case, the Pythia samples have considerably higher purity than both Herwig samples, as can be seen in Fig. 6.9b. This can be immediately understood by observing Fig. 6.5, since only the leptonic b jet is contained in the leptonic top construction and Pythia has much fewer events with missing b jets compared to Herwig.

6.2.2 Selection Cuts based on SPANet

Finally a SPANet cut on the hadronic top existence score will be applied to reco-level events to determine how the kinematics of each SMC program change with higher reconstruction purity. The selection will exclude any event that is not within the *high* existence, i.e. t^{had} score > 0.5 is required to pass the event selection. The kinematics are plotted in
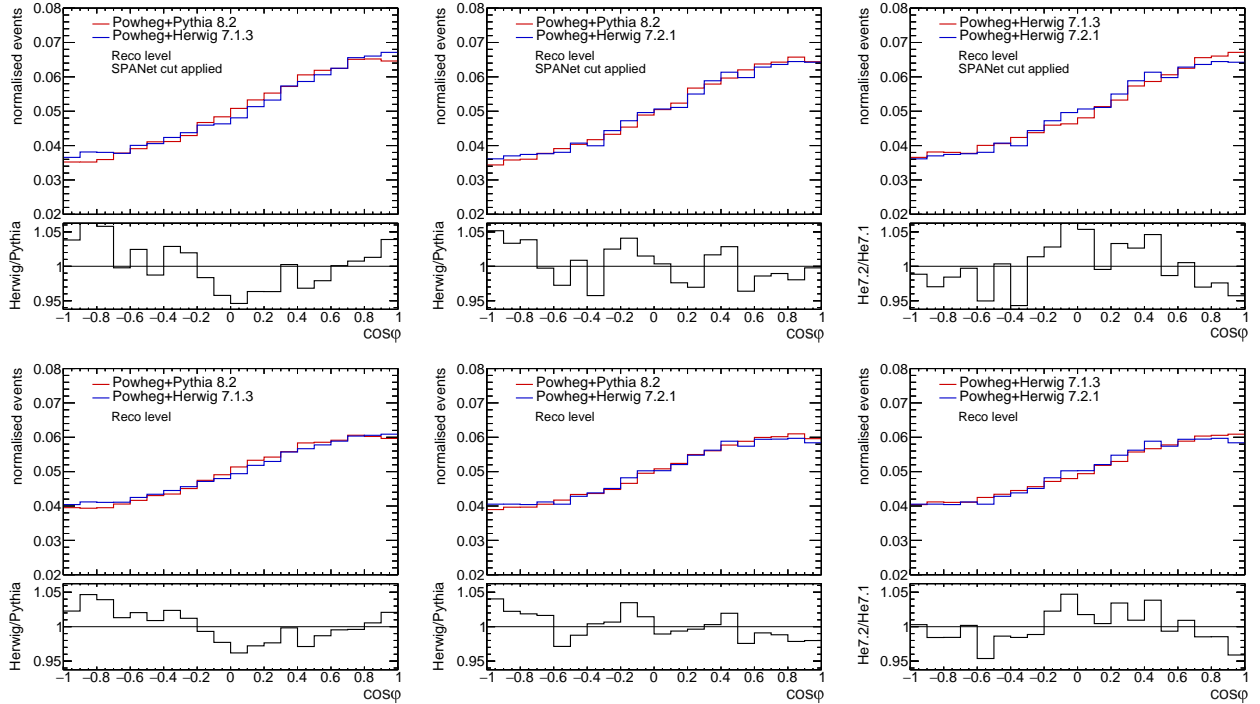
Abb. 6.13: Normalised $\cos\varphi$ distributions on reco-level for POWHEG+HERWIG 7.1.3, POWHEG+HERWIG 7.2.1 and POWHEG+PYTHIA 8.2 with a cut on the hadronic top existence variable from SPANet on the top and without on the bottom.

Figures 6.14, 6.15, 6.16, 6.17, and 6.18, where each figure includes the kinematics without the SPANet cut for the sake of comparability. The ratios between the samples remain almost the same but the distributions are shifted towards a higher p_T. This is especially noticeable in the up and down jet distributions. Also the percentage of events with more than four jets increased as well. Table 6.2 shows the results for the D value compared to without the extra SPANet cut. The systematic uncertainties went down for both, the fast simulation and the full simulation pair of samples. The HERWIG 7.1.3 sample maintains a smaller difference to the PYTHIA sample compared to HERWIG 7.2.1. Also the D values of both HERWIG samples still lie within 1% of each other. The D values both increased by 38% in magnitude, which brings them closer to their particle-level value. In return, the statistics decrease by over 40% for each sample as shown in Table 6.3, which introduces greater statistical uncertainty into the shapes of the $\cos\varphi$ distributions.
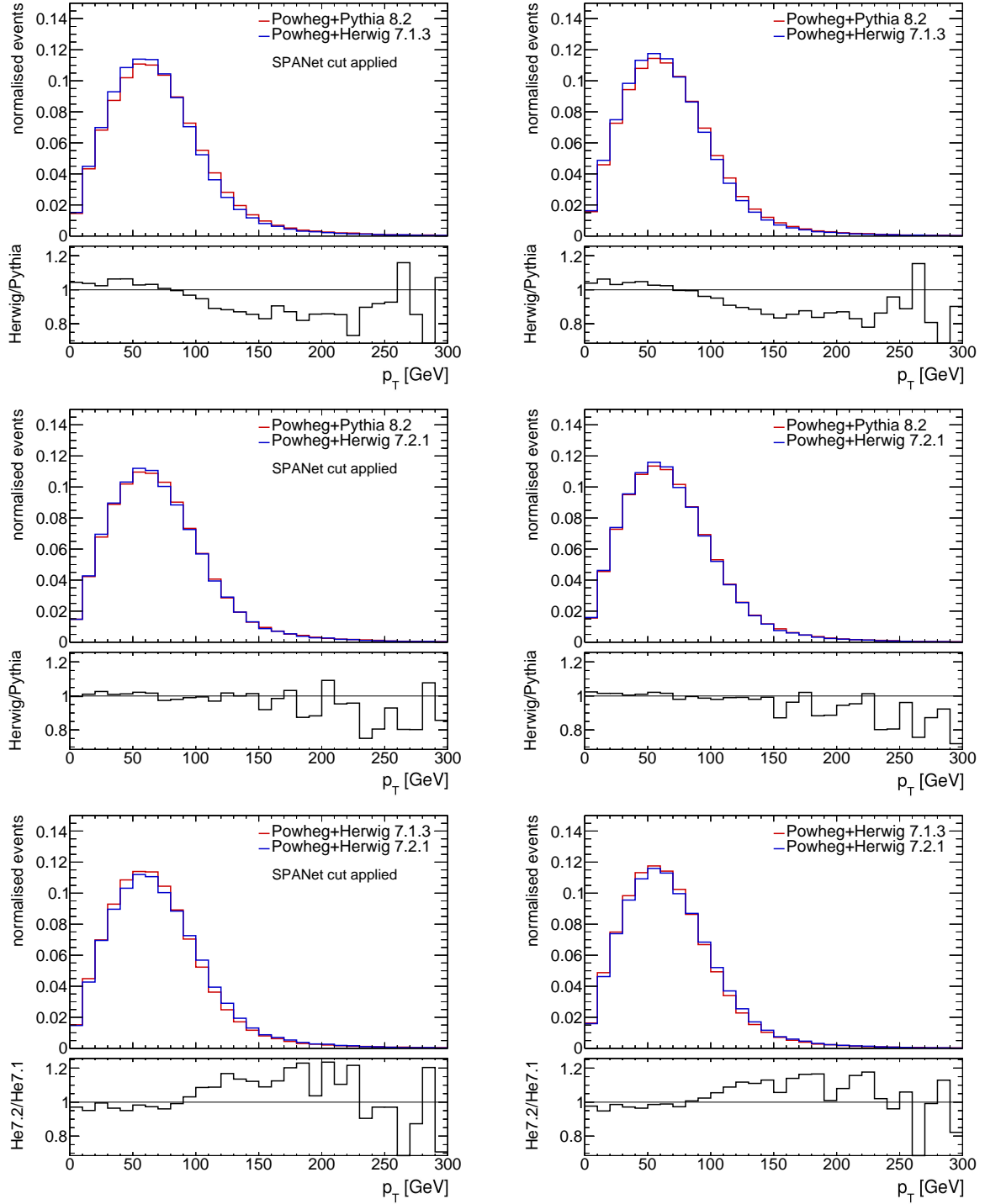
Abb. 6.14: Normalised p_T distributions of the hadronic top for POWHEG+HERWIG 7.1.3, POWHEG+HERWIG 7.2.1, and POWHEG+PYTHIA 8.2 with a cut on the hadronic top existence variable from SPANet on the left and without on the right.
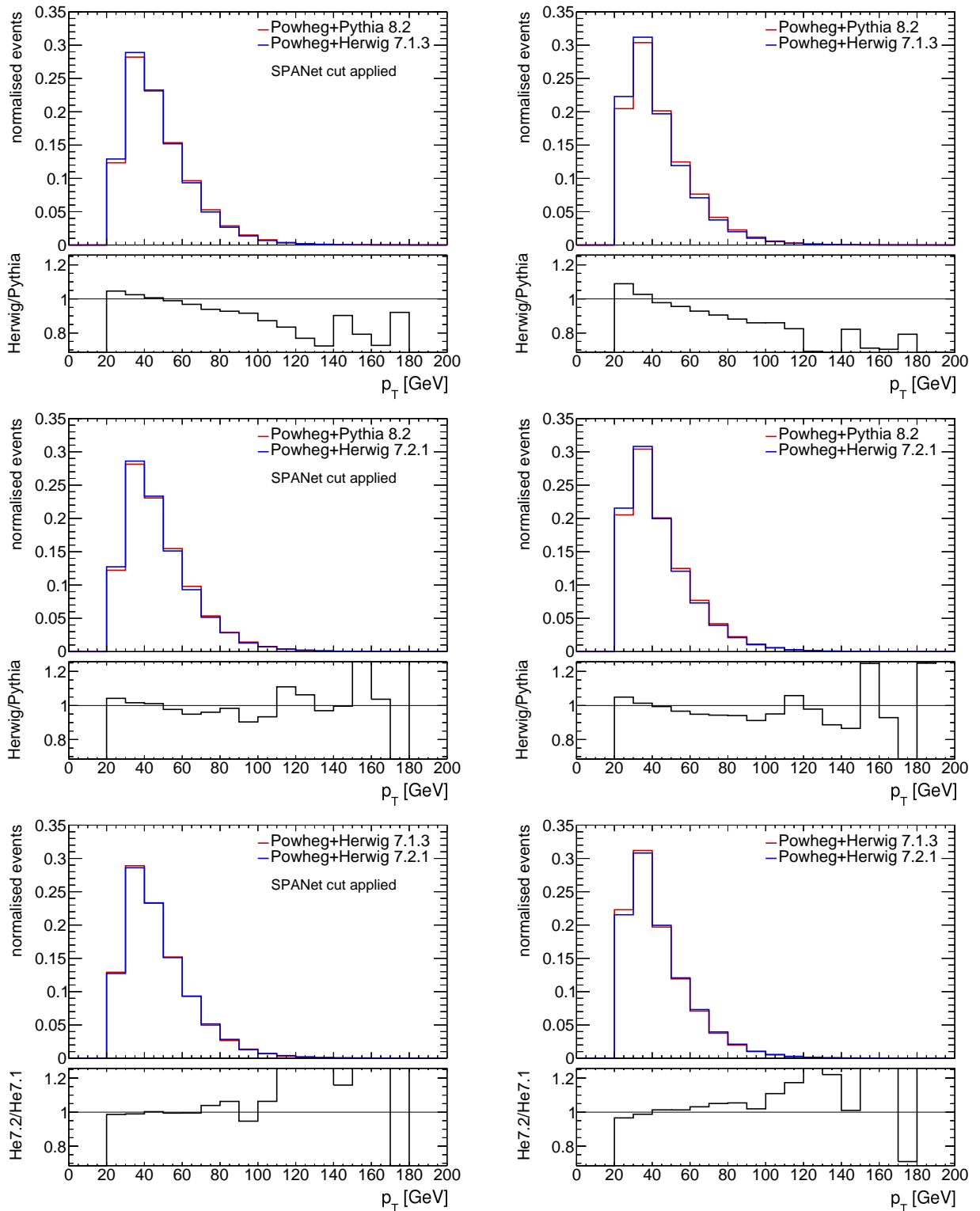
Abb. 6.15: Normalised p_T distributions of the down type jet for Powheg+Herwig 7.1.3, Powheg+Herwig 7.2.1, and Powheg+Pythia 8.2 with a cut on the hadronic top existence variable from SPANet on the left and without on the right.
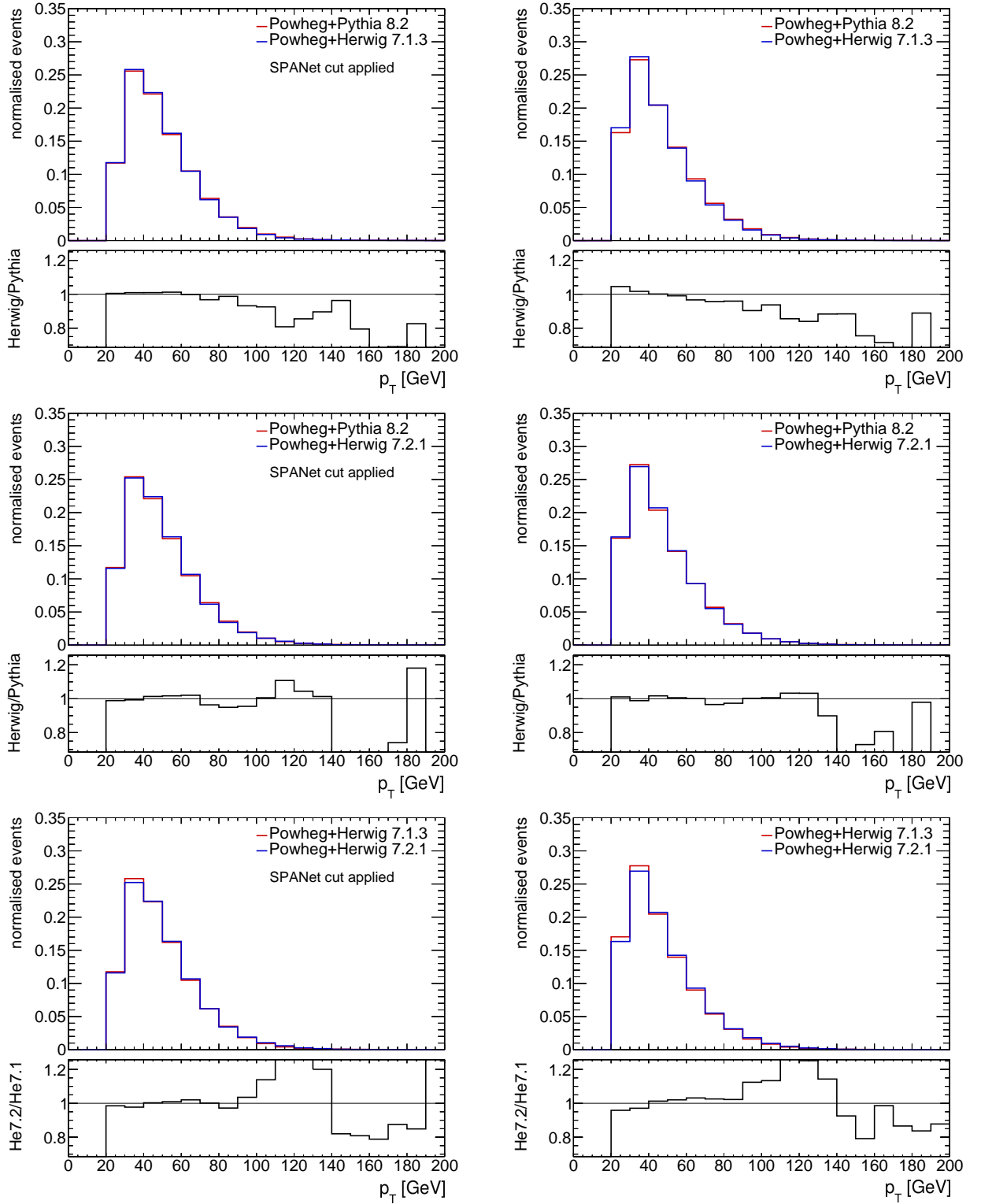
Abb. 6.16: Normalised p_T distributions of the up type jet for POWHEG+HERWIG 7.1.3, POWHEG+HERWIG 7.2.1, and POWHEG+PYTHIA 8.2 with a cut on the hadronic top existence variable from SPANet on the left and without on the right.
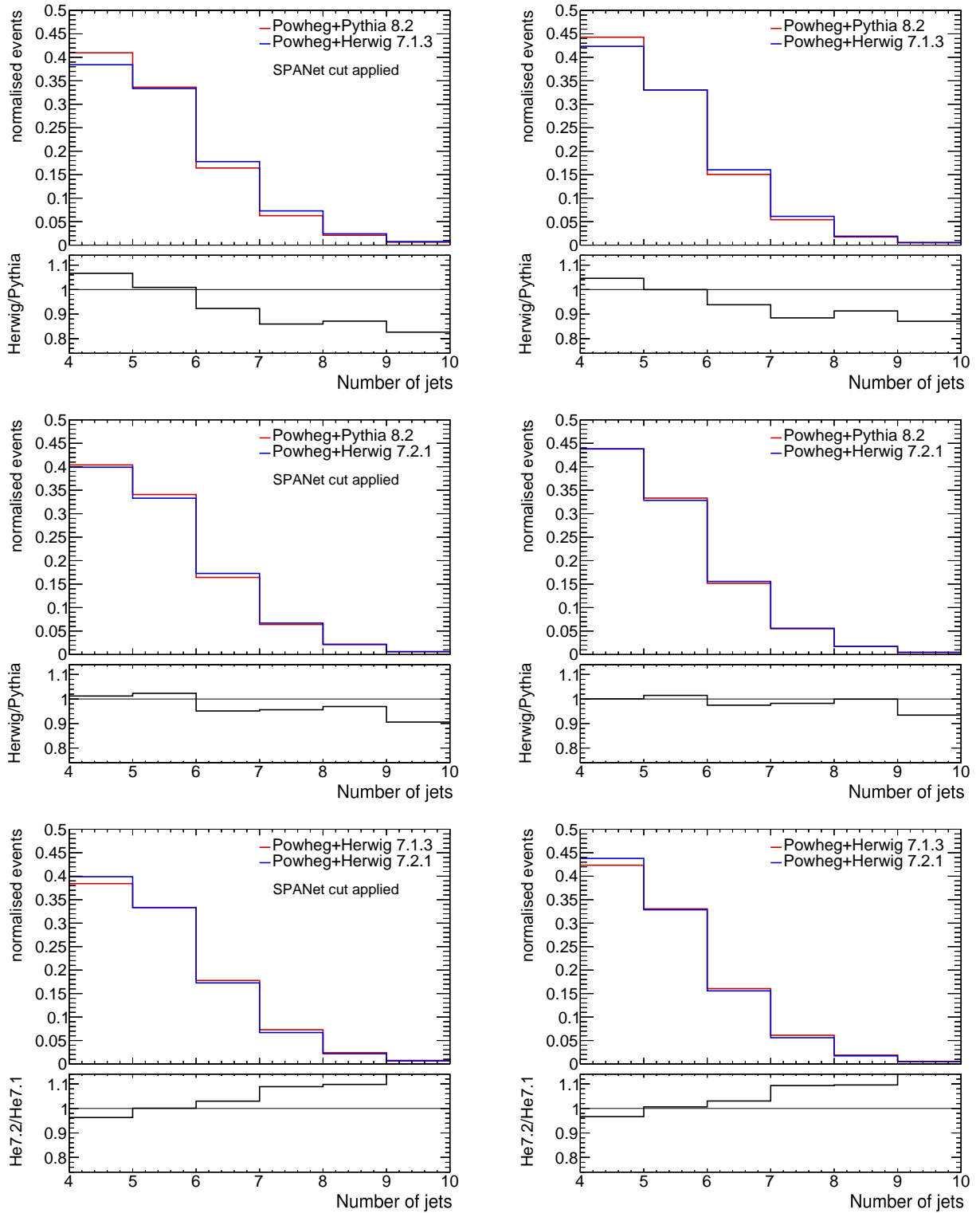
Abb. 6.17: Normalised distribution of the total number of jets in a given event for
Powheg+Herwig 7.1.3, Powheg+Herwig 7.2.1, and Powheg+Pythia
8.2 (fastsim) with a cut on the hadronic top existence variable from SPANet
on the left and without on the right.
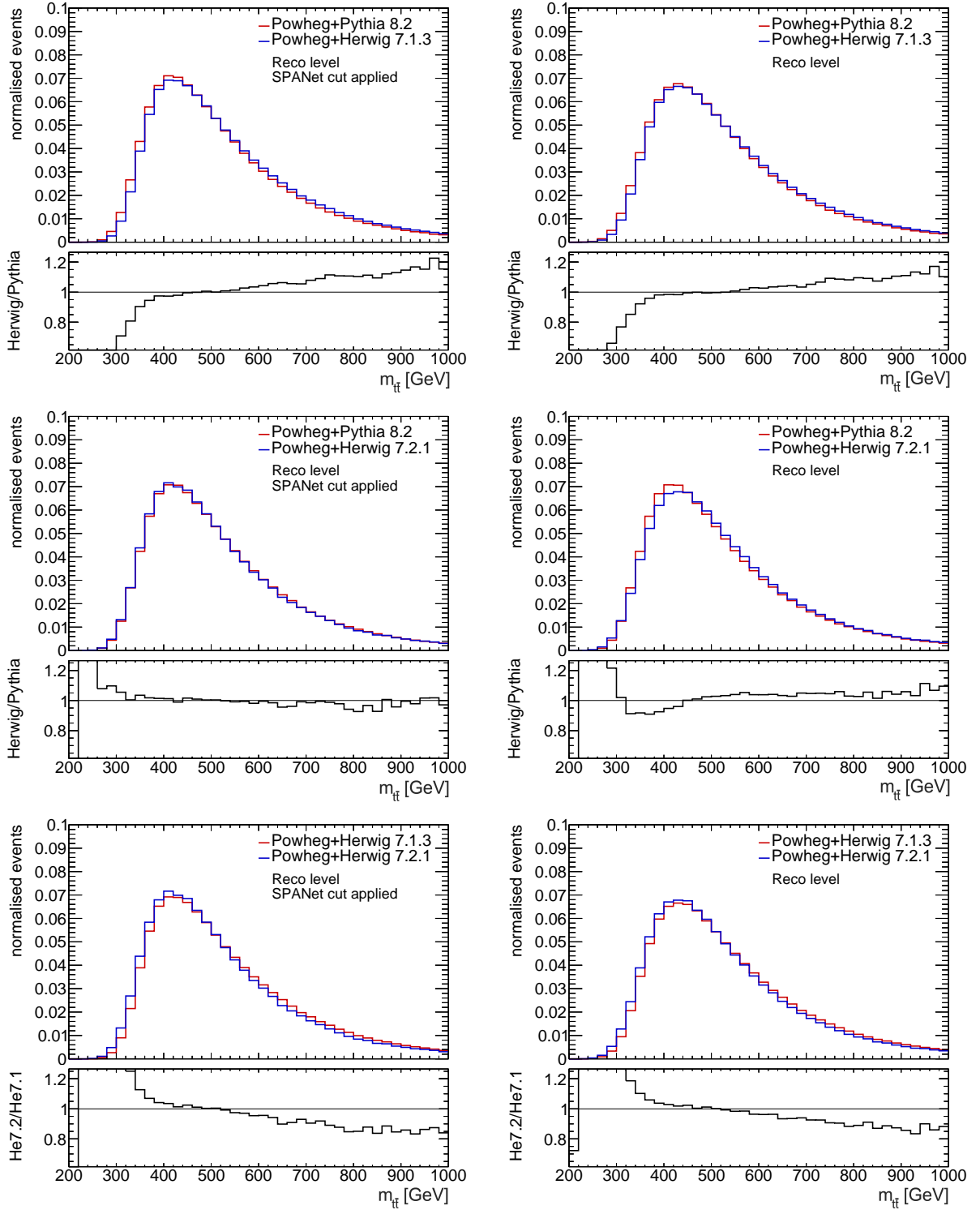
Abb. 6.18: Normalised $m_{t\bar{t}}$ distributions on reco-level for POWHEG+HERWIG 7.1.3, POWHEG+HERWIG 7.2.1 and POWHEG+PYTHIA 8.2 with a cut on the hadronic top existence variable from SPANet on the left and without on the right.

7 Summary & Conclusion

In this thesis, a spin observable $\cos\varphi$ was introduced to access entanglement in top quark pairs. The analysis focused on the lepton+jets decay channel. A c-tagging approach was used in the identification of the hadronic spin analyzer while the jet-parton matching of the event reconstruction was handled by the SPANet neural network. The Monte Carlo samples were produced using the different Shower Monte Carlo generators HERWIG 7.1.3 or HERWIG 7.2.1 and PYTHIA 8.2 matched to POWHEG for NLO corrections. The differences in the particle-level shape of the $\cos\varphi$ distribution that originate from a calculation using different SMC programs constitute a source of substantial systematic uncertainties in this analysis. The kinematics of the physics objects used in the calculation were compared to make sense of the systematic uncertainties. Also the reconstruction with SPANet was examined in greater detail.

Table 6.1 shows the results of the analysis for the D values, which are a direct entanglement measure, extracted from the $\cos\varphi$ distribution. On parton-level, all samples fullfill the entanglement criterion $D < -1/3$. The modelling of the parton shower and subsequent hadronisation on particle level introduces major differences into the $\cos\varphi$ and the resulting D values. Particle-level jet-parton matching is substantially more accurate for the PYTHIA sample than for the HERWIG samples. Therefore the jet carrying the correct angular information is chosen a lot more often with PYTHIA. In general, the different kinematic distrutions of the newer HERWIG 7.2.1 program show better agreement with PYTHIA compared to the older HERWIG 7.1.3 program, reducing the particle-level systematic uncertainties considerably. In conclusion, the use of HERWIG 7.2.1 version is to be preferred over HERWIG 7.1.3 in this particular analysis.

The SPANet reconstruction assigns scores to each event, that are correlated to the purity of the reconstruction of either the hadronic or leptonic top. For the hadronic top, the distributions of correctly matched and non-reconstructable events are shifted apart. This allows the introductions of different regions with predominantly non-reconstrucatble events. Applying a selection cut based on these regions, reduces the deviation between the particle-level and reco-level D values by $38\,\%$ for all samples and additionally reduces the difference of the kinematic variables an event between the different SMC programs.

Literaturverzeichnis

[1] P. W. Higgs, *Spontaneous Symmetry Breakdown without Massless Bosons*, Phys. Rev. **145**, 1156 (1966)

[2] P. W. Higgs, *Broken Symmetries and the Masses of Gauge Bosons*, Phys. Rev. Lett. **13**, 508 (1964)

[3] G. S. Guralnik, C. R. Hagen, T. W. B. Kibble, *Global Conservation Laws and Massless Particles*, Phys. Rev. Lett. **13**, 585 (1964)

[4] T. W. B. Kibble, *Symmetry Breaking in Non-Abelian Gauge Theories*, Phys. Rev. **155**, 1554 (1967)

[5] M. Drewes, *The Phenomenology of Right Handed Neutrinos*, Int. J. Mod. Phys. E **22**, 367 (2013)

[6] S. Willenbrock, *Symmetries of the Standard Model*, arXiv:hep-ph/0410370 (2008)

[7] G. 't Hooft, M. Veltman, *Regularization and renormalization of gauge fields*, Nucl. Phys. B **44(1)**, 189 (1972)

[8] G. 't Hooft, *Renormalizable Lagrangians for massive Yang-Mills fields*, Nucl. Phys. B **35(1)**, 167 (1971)

[9] S. Weinberg, *A model of leptons*, Phys. Rev. Lett. **19** (1967)

[10] A. Salam, *Weak and Electromagnetic Interactions*, Conf.Proc.C **680519**, 367 (1968)

[11] M. Kobayashi, T. Maskawa, *CP Violation in the Renormalizable Theory of Weak Interaction*, Prog. Theor. Phys. **49**, 652 (1973)

[12] H. Pérez, et al., *Cabibbo-Kobayashi-Maskawa matrix: parameterizations and rephasing invariants*, J. Phys.: Conf. Ser. **485**, 012058 (2014)

[13] F. Englert, R. Brout, *Broken Symmetry and the Mass of Gauge Vector Mesons*, Phys. Rev. Lett. **13**, 321 (1964)

[14] H. D. Politzer, *Asymptotic Freedom: An Approach to Strong Interactions*, Phys. Rept. **14** (1974)

[15] W. J. Marciano, H. Pagels, *Quantum Chromodynamics: A Review*, Phys.Rept. **36** (1978)

[16] K. G. Wilson, *Confinement of Quarks*, Phys. Rev. D **10**, 2445 (1974)

[17] F. Wilczek, *Quantum Chromodynamics (QCD): The Modern Theory of the Strong Interaction*, Ann. Rev. Nucl. Part. Sci. **32**, 177 (1982)

[18] D. J. Gross, F. Wilczek, *Ultraviolet behavior of non-abelian gauge theories*, Phys. Rev. Lett. **44(1)**, 1343 (1973)

[19] M. Kobayashi, T. Maskawa, *CP Violation in the Renormalizable Theory of Weak Interaction*, Prog. Theor. Phys. **49**, 652 (1973)

[20] R. Workman, et al. (Particle Data Group), *Review of Particle Physics*, Prog. Theor. Exp. Phys. **2022**, 083C01 (2022)

[21] F. Abe, et al. (CDF Collaboration), *Observation of Top Quark Production in $\bar{p}p$ Collisions*, Phys. Rev. Lett. **74**, 2626 (1995)

[22] S. Abachi, et al. (DØ Collaboration), *Observation of the Top Quark*, Phys.Rev.Lett. **74**, 2632 (1995)

[23] A. Peres, *Separability Criterion for Density Matrices*, Phys. Rev. Lett. **77**, 1413 (1996)

[24] P. Horodecki, *Separability criterion and inseparable mixed states with positive partial transposition*, Physics Letters A **232(5)**, 333 (1997)

[25] Y. Afik, J. R. M. de Nova, *Entanglement and quantum tomography with top quarks at the LHC*, Eur. Phys. J. Plus **136(9)** (2021)

[26] M. Sirunyan, et al. (CMS Collaboration), *Measurement of the top quark polarization and $t\bar{t}$ spin correlations using dilepton final states in proton-proton collisions at $\sqrt{s} = 13$ TeV*, Phys. Rev. D **100(7)** (2019)

[27] G. Mahlon, S. J. Parke, *Spin correlation effects in top quark pair production at the LHC*, Phys. Rev. D **81(7)** (2010)

[28] F. Hubaut, et al., *ATLAS sensitivity to top quark and W boson polarization in $t\bar{t}$ events*, Eur. Phys. J. C **44(S1)**, 13 (2005)

[29] W. Bernreuther, et al., *A set of top quark spin correlation and polarization observables for the LHC: Standard Model predictions and new physics contributions*, JHEP **2015(12)**, 1 (2015)

[30] T.-M. Yan, S. D. Drell, *The parton model and its applications*, Int. J. Mod. Phys. A **29(30)**, 1430071 (2014)

[31] D. E. Soper, *Parton distribution functions*, Nucl. Phys. B **53(1-3)**, 69 (1997)

[32] J. C. Collins, et al., *Factorization of Hard Processes in QCD*, Adv.Ser.Direct.High Energy Phys. **5**, 1 (1989)

[33] J. Collins, et al., *The Theorems of Perturbative QCD*, Ann. Rev. Nucl. Part. Sci. **37**, 383 (1987)

[34] M. Bähr, et al, *Herwig physics and manual*, Eur. Phys. J. C **58(4)**, 639 (2008)

[35] T. Sjöstrand, S. Mrenna, P. Skands, *PYTHIA 6.4 physics and manual*, JHEP **2006(05)**, 026 (2006)

[36] V. V. Sudakov, *Vertex parts at very high-energies in quantum electrodynamics*, Sov. Phys. JETP **3**, 65 (1956)

[37] S. Ferreres-Solé, T. Sjöstrand, *The space–time structure of hadronization in the Lund model*, Eur. Phys. J. C **78(11)** (2018)

[38] J.-C. Winter, et al., *A modified cluster-hadronisation model*, Eur. Phys. J. C **36(3)**, 381 (2004)

[39] L. G. Almeida, et al., *Substructure of high-p_T jets at the LHC*, Phys. Rev. D **79(7)** (2009)

[40] A. J. Larkoski, et al., *Jet substructure at the Large Hadron Collider: A review of recent advances in theory and machine learning*, Phys. Rep. **841**, 1 (2020)

[41] S. Weinzierl, *The SISCone jet algorithm optimised for low particle multiplicities*, Comput. Phys. Commun. **183(3)**, 813 (2012)

[42] S. Catani, et al., *Longitudinally invariant K_t clustering algorithms for hadron hadron collisions*, Nucl. Phys. B **406**, 187 (1993)

Literaturverzeichnis

[43] M. Cacciari, et al., *The anti-k_T jet clustering algorithm*, JHEP **2008(04)**, 063 (2008)

[44] M. Sirunyan, et al. (CMS Collaboration), *A Cambridge-Aachen (C-A) based Jet Algorithm for boosted top-jet tagging* **CMS-PAS-JME-09-001** (2009)

[45] R. Atkin, *Review of jet reconstruction algorithms*, J. Phys.: Conf. Ser. **645(1)**, 012008 (2015)

[46] L. Evans, P. Bryant, *Review of Particle Physics*, JINST **3**, S08001 (2008)

[47] G. Apollinari, et al., *High Luminosity Large Hadron Collider HL-LHC*, CERN Yellow Report **CERN-2015-005** (2017)

[48] G. Aad, et al. (ATLAS Collaboration), *The ATLAS Experiment at the CERN Large Hadron Collider*, JINST **3**, S08003 (2008)

[49] A. Buckley, et al., *General-purpose event generators for LHC physics*, Phys. Rep. **504(5)**, 145 (2011)

[50] S. Agostinelli, et al. (Geant4 Collaboration), *GEANT4: A Simulation Toolkit*, Nucl. Instrum. Methods A **506**, 250 (2003)

[51] A. Basalaev, et al., *The Fast Simulation Chain for ATLAS*, J. Phys.: Conf. Ser. **898**, 042016 (2017)

[52] T. Sjöstrand, et al., *An introduction to PYTHIA 8.2*, Comput. Phys. Commun. **191**, 159 (2015)

[53] T. Sjöstrand, P. Z. Skands, *Transverse-momentum-ordered showers and interleaved multiple interactions*, Eur. Phys. J. C **39(2)**, 129 (2005)

[54] M. Cacciari, G. P. Salam, G. Soyez, *FastJet user manual*, Eur. Phys. J. C **72(3)** (2012)

[55] J. Bellm, et al., *Herwig 7.0/Herwig 3.0 release note*, Eur. Phys. J. C **76(4)** (2016)

[56] J. Bellm, et al., *Herwig 7.1 Release Note,* **CERN-PH-TH-2017-109** (2017)

[57] J. Bellm, et al., *Herwig 7.2 Release Note*, Eur. Phys. J. C **80(5)** (2020)

[58] C. Oleari, *The POWHEG BOX*, Nucl. Phys. B **205-206**, 36 (2010)

[59] S. Frixione, P. Nason, C. Oleari, *Matching NLO QCD computations with parton shower simulations: the POWHEG method*, JHEP **2007(11)**, 070 (2007)

[60] A. Buckley, D. B. Gupta, *Powheg-Pythia matching scheme effects in NLO simulation of dijet events*, arXiv:1608.03577v4 [**hep-ph**] (2017)

[61] G. Aad, et al. (ATLAS Collaboration), *ATLAS flavour-tagging algorithms for the LHC Run 2 pp collision dataset*, Eur. Phys. J. C **83(681)** (2023)

[62] G. Aad, et al. (ATLAS Collaboration), *ATLAS b-jet identification performance and efficiency measurement with $t\bar{t}$ events in pp collisions at $\sqrt{s} = 13$ TeV*, Eur. Phys. J. C **79(11)** (2019)

[63] A. Shmakov, et al., *SPANet: Generalized permutationless set assignment for particle physics using symmetry preserving attention*, SciPost Phys. **12**, 178 (2022)

[64] M. J. Fenton, et al., *Permutationless many-jet event reconstruction with symmetry preserving attention networks*, Phys. Rev. D **105**, 112008 (2022)

[65] G. Aad, et al. (ATLAS Collaboration), *Proposal for particle-level object and observable definitions for use in physics measurements at the LHC* **ATL-PHYS-PUB-2015-013** (2015)

[66] G. Aad, et al. (ATLAS Collaboration), *Differential top-antitop cross-section measurements as a function of observables constructed from final-state particles using pp collisions at $\sqrt{s} = 7$ TeV in the ATLAS detector*, JHEP **2015(6)** (2015)

[67] L. Lista, *Practical Statistics for Particle Physicists*, CERN Yellow Reports: School Proceedings pages Vol 5 (2017): Proceedings of the 2016 European School of High–Energy Physics (2017)

Acknowlegements

Erklärung nach §13(9) der Prüfungsordnung für den Bachelor-Studiengang Physik und den Master-Studiengang Physik an der Universität Göttingen: Hiermit erkläre ich, dass ich diese Abschlussarbeit selbständig verfasst habe, keine anderen als die angegebenen Quellen und Hilfsmittel benutzt habe und alle Stellen, die wörtlich oder sinngemäß aus veröffentlichten Schriften entnommen wurden, als solche kenntlich gemacht habe.

Darüberhinaus erkläre ich, dass diese Abschlussarbeit nicht, auch nicht auszugsweise, im Rahmen einer nichtbestandenen Prüfung an dieser oder einer anderen Hochschule eingereicht wurde.

Göttingen, den 24. Oktober 2023

(Tobias Henne)